Laves phase field in a diblock copolymer alloy

Benjamin R. Magruder, So Jung Park, Ryan P. Collanton, Frank S. Bates, and Kevin D. Dorfman*

Department of Chemical Engineering and Materials Science, University of Minnesota – Twin Cities, 421 Washington Ave SE, Minneapolis, Minnesota 55455, USA

E-mail: dorfman@umn.edu

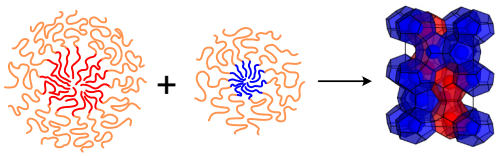

for Table of Contents use only

Abstract

Laves phases are a class of tetrahedrally close-packed Frank Kasper phases with AB_2 stoichiometry. While these phases appear as intermetallic line compounds in a variety of metallic alloys, it is challenging to stabilize Laves phases in reconfigurable soft matter owing to the substantial difference in preferred volume between the large A particles and small B particles. Surprisingly, perhaps the conceptually simplest approach — blending two diblocks with incompatible core blocks — has not been explored yet. Using self-consistent field theory, we predict that a Laves phase should emerge as a phase field in the eutectic phase diagram of an AB/B′C diblock copolymer blend if (i) the AB and B′C diblock copolymers are selected such that their neat melts produce bcc phases with the particle volume ratio of the desired Laves phase and (ii) the repulsion

*To whom correspondence should be addressed

between A and C blocks is sufficiently strong to minimize mixing between micelles. This diblock "alloying" approach produces phase behavior that closely mimics that arising in intermetallic compound-producing metal alloys, and should provide a relatively simple synthetic route to produce soft Frank-Kasper phases that are challenging to achieve by conventional polymer-based approaches.

Introduction

Binary metallic alloys exhibit a wide range of phase behavior, including liquids, solid solutions, and two- and three-phase equilibrium. Of particular interest are intermetallic compounds, which have distinct stoichiometries[1] and thus differ qualitatively from the continuously varying compositions exhibited by solid solutions. In the ideal case, an intermetallic compound appears in the phase diagram as a line compound at the composition corresponding to its stoichiometry; non-ideal systems can produce a narrow composition window known as a phase field.[2] Laves phases are one important class of intermetallic compounds, exemplified by the C14 and C15 phases illustrated in Fig. 1a. Laves phases are a subset of tetrahedrally close-packed Frank-Kasper phases[3,4] with an AB_2 stoichiometry. The smaller, 12-fold coordinated B particles are arranged on a 2D Kagome net layered with a triangulated net of the larger, 16-fold coordinated A particles, another triangulated net of B particles, and a third of A particles.[4] This complexity contrasts sharply with a body-centered cubic (bcc) phase, for example, which contains two identical particles per conventional unit cell (Fig. 1b). Owing to their ability to accommodate two differently sized atoms, Laves phases are the largest group of intermetallic compounds, with the canonical examples being $MgZn_2$ (C14), $MgCu_2$ (C15), and $MgNi_2$ (C36).[5]

Packing on lattices is also observed when flexible, compositionally asymmetric diblock copolymers, which aggregate into micellar particles, are cooled below the order-disorder transition. In contrast to metal alloys, where the ordered state symmetry is governed by a combination of atomic packing and electronic interactions, the thermodynamics governing

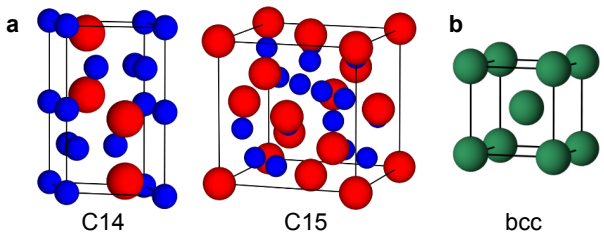

Figure 1: Schematic of the (a) C14 ($MgZn_2$) and C15 ($MgCu_2$) Laves phases and (b) bcc phase. For the Laves phases, the larger A particles are red, and the smaller B particles are blue. Created using a modification of the program provided in Ref. 6.

the phase behavior of block polymer melts is markedly simpler. Here, the selection of the ordered state is governed by a competition between chain stretching and interfacial tension subject to the constraint of constant density, and thus exposes the geometric role of particle packing on the selection of ordered state symmetry. While bcc is the most commonly observed particle packing in block polymer melts, various Frank-Kasper phases have been observed as well,[7–22] consistent with their emergence in other forms of soft matter.[23–31] However, Laves phases are much less commonly observed in diblock copolymer melts[17–22] than other Frank-Kasper phases, and theory predicts that only the C14 and C15 Laves phases are likely to be stable.[32] Moreover, the Laves phases seen to date appear in block polymer phase diagrams as stability windows rather than the line compounds that emerge for intermetallic compounds. In the present contribution, we describe an approach, inspired by metallic alloys and supported by self-consistent field theory (SCFT) calculations, that promotes the formation of block copolymer Laves phases as a phase field (i.e., a non-ideal line compound) within a eutectic phase diagram that closely mimics that observed for metal alloys.

To understand the need for our approach, it is useful to recall first existing methods to produce Laves phases in diblock copolymers. Theory predicts that Laves phases are metastable in neat melts, owing to the entropically unfavorable chain stretching needed to accommodate the particle volume asymmetry of the structures.[17,18] However, for neat block copolymers melts, Laves phases have been formed via thermal processing routes[17–19,22] that presumably leverage the intrinsic distribution of micelle volumes in the liquid-like packing state, which

emerges upon deep cooling, to promote subsequent ordering into a Laves phase after reheating. These are inherently non-equilibrium processes whose molecular mechanisms are not well understood.[33] Laves phases have also been observed as equilibrium states in diblock copolymer/homopolymer blends,[8,20] where the nonuniform loading of homopolymer into the micelle core allows the system to accommodate the particle volume asymmetry. While the underlying molecular mechanism for Frank-Kasper phase formation in these blends appears to be understood[20,34,35] and the resulting Laves phases are equilibrium states, blending with homopolymers is not a particularly robust approach due to macrophase separation as the homopolymer volume fraction increases, and it is not obvious how to target a particular Frank-Kasper phase. Finally, C14 has been observed in AB/A′B blends,[21] where the prime denotes a different degree of polymerization. Relying on SCFT, several molecular mechanisms have been proposed for stabilizing Laves phases in AB/A′B systems including domain segregation[36] and delocalization of the smaller chains from the interface.[21] However, much of the Laves phase region predicted by SCFT for one AB/A′B blend was not realized experimentally.[21] Moreover, the domain segregation mechanism,[37] which is a powerful approach to produce Frank-Kasper phases in blends,[15] tends to favor forming interfaces of different curvature but does not necessarily promote volume asymmetry. Thus, we were interested in whether we could develop a more general approach for block polymers that would provide a rational route to design systems that will favor the formation of Laves phases and thus provide a soft matter equivalent to phase diagrams for alloys that form intermetallic phases.

Methods

Figure 2 illustrates our approach based on using an AB/B′C blend. A literature on such blends has accumulated gradually over the past three decades,[38–53] much of it focused on the competition between microphase and macrophase separation using experiments coupled to random-phase approximation (RPA) calculations of spinodal lines,[40–44] creating composite

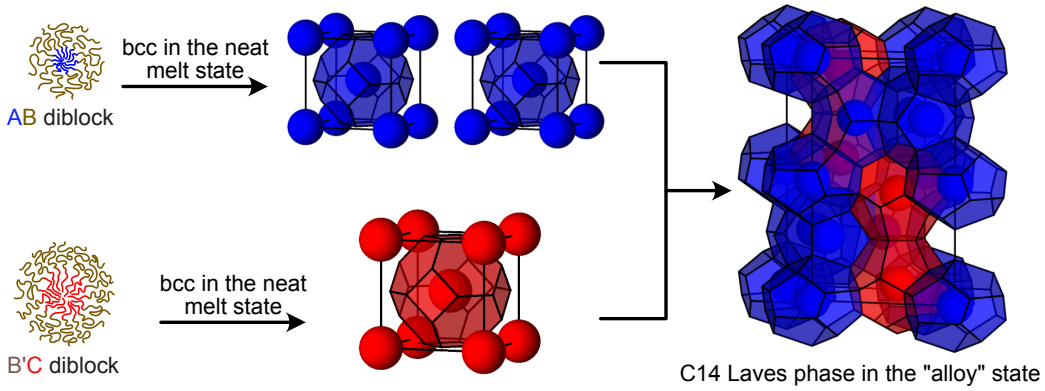

Figure 2: Principle of the block polymer alloying method to stabilize Laves phases. By selecting χ_{AC} to be sufficiently high, a blend of compositionally asymmetric AB and B′C diblock copolymers will produce two different micellar particle sizes. The degrees of polymerization $N_{AB} < N_{B'C}$ are selected such that the particles formed in their respective neat bcc melts correspond to the volume asymmetry of the Laves phase. When mixed with approximately the 2:1 stoichiometry, the Laves phase is predicted to emerge. The enclosing polyhedra correspond to the Voronoi construct and were created using the program provided in Ref. 6.

continuous phases for nanoporous materials when the A and C blocks are miscible,[47–49] or promoting the formation of unconventional morphologies.[50–53] To produce a Laves phase in the AB/B′C system, we first selected the volume fraction f_A of the A-block to be small, which will produce micellar particles provided the segregation strength $\chi_{AB}N_{AB}$ is above the order-disorder transition value, where χ_{AB} is the Flory-Huggins parameter between blocks A and B and N_{AB} is the degree of polymerization of the AB polymer. For notational simplicity going forward, let us denote the segregation strength between blocks i and j in a chain of size N in the compact form $(\chi N)_{ij}$. We further select f_C and $(\chi N)_{B'C}$ to promote formation of micelles in B′C as well. To produce two distinct particle sizes, we require $N_{AB} < N_{B'C}$ and that χ_{AC} be sufficiently large to suppress mixing of the AB polymers in the B′C micelles and vice versa.[39] We then anticipate the system will order into a Laves phase if (i) the blend volume fractions ϕ_{AB} and $\phi_{B'C} = 1 - \phi_{AB}$ produce particles at approximately a 2:1 stoichiometry and (ii) the choices for N_{AB} and $N_{B'C}$ lead to micelles with the Laves volume asymmetry.

With these general principles in mind, we describe how to implement this strategy in

practice. This initial communication focuses on a relatively simple system. First, we set the statistical segment lengths for each block to the same value b, removing the effect of conformational asymmetry that, on its own, tends to aid Frank-Kasper phase formation.[54] Second, we designed our system around the bcc particles formed at $(\chi N)_{\mathrm{AB}} = (\chi N)_{\mathrm{B'C}} = 25$, with $\chi_{\mathrm{AC}} N_{\mathrm{AB}} = 50$ to suppress the mixing of micelles. From the classic SCFT results for conformationally symmetric diblock copolymers,[55] the choice $f_{\mathrm{A}} = f_{\mathrm{C}} = 0.2$ is inside the bcc region of the phase diagram for neat melts at $\chi N = 25$. The bcc system has two particles in a unit-cell volume that scales as $N^{3/2}$ for a fixed χN and minority block volume fraction. Thus, if we desire a ratio α between the particle volumes for $(\chi N)_{\mathrm{AB}} = (\chi N)_{\mathrm{B'C}}$ and $f_{\mathrm{A}} = f_{\mathrm{C}}$, we should select $N_{\mathrm{B'C}}/N_{\mathrm{AB}} = \alpha^{2/3}$, where we have chosen arbitrarily that B′C form the larger particles. In this model, the Laves phase should appear at $\phi_{\mathrm{AB}} \approx 2/(2+\alpha)$.

To investigate the feasibility of this approach, we have studied the block polymer alloy using SCFT for a Gaussian chain model. All calculations were performed using the open-source Polymer Self Consistent Field (PSCF) software package in either canonical and grand canonical ensembles.[56–58] Canonical ensemble calculations employed the original Fortran version of this program[57] while the grand canonical ensemble calculations used the C++ version.[34] Additional information on these calculations and the approach to compute the phase equilibria are provided in the Supporting Information.

Results

The precise volume asymmetry α is not known, so we used canonical ensemble SCFT calculations in the PSCF software package[57] to compute the free energies of the AB-rich bcc phase, the B′C-rich bcc phase, and the C15 Laves phase as a function of the volume fraction ϕ_{AB} of the AB block polymer in the blend for $N_{\mathrm{B'C}}/N_{\mathrm{AB}} = 1$ to $N_{\mathrm{B'C}}/N_{\mathrm{AB}} = 1.5$ with the aforementioned segregation strengths. These bcc phases are comprised of micelles of the majority component at the lattice sites, with the minority component at the interstitial sites.

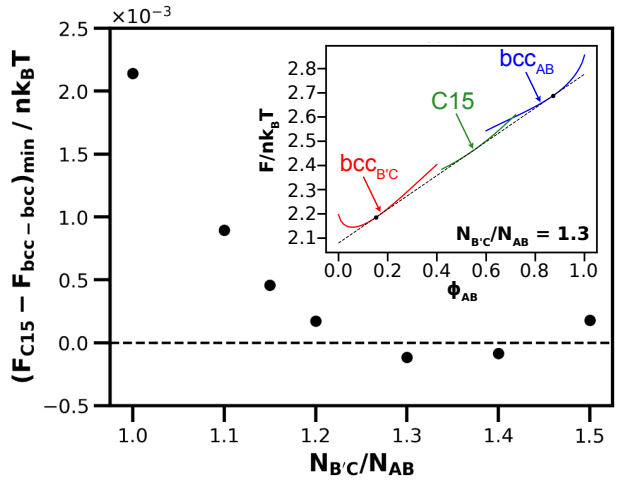

Figure 3: Free energy per chain of size N_{AB} of the C15 Laves phase relative to the free energy of a macrophase separated mixture of AB-rich bcc and B′C-rich bcc as a function of the relative degree of polymerization of the AB and B′C polymers for $(\chi N)_{\mathrm{AB}} = (\chi N)_{\mathrm{BC}} = 25$, $\chi_{\mathrm{AC}} N_{\mathrm{AB}} = 50$, and $f_{\mathrm{A}} = f_{\mathrm{C}} = 0.2$. The data points correspond to the minimum of the free energy difference. The inset provides an example of the underlying free energy diagram versus volume fraction of AB and the double-tangent construction for the polymerization ratio $N_{\mathrm{B'C}}/N_{\mathrm{AB}} = 1.3$. The corresponding data for other values of $N_{\mathrm{B'C}}/N_{\mathrm{AB}}$ are provided as Fig. S2.

The choice of C15 (versus C14) for the present purposes is arbitrary as these two phases are nearly degenerate in free energy as shown in prior work,[17,18,32,59] and that proves to be the case here too (Fig. S10).

The inset of Fig. 3 provides an exemplary result obtained for $N_{\mathrm{B'C}}/N_{\mathrm{AB}} = 1.3$, illustrating the free energy per chain of length N_{AB} as a function of the volume fraction ϕ_{AB} in the melt. Companion data for other values of $N_{\mathrm{B'C}}/N_{\mathrm{AB}}$ are provided in Fig. S2. Owing to the different sizes of the AB and B′C polymers, the bcc-bcc tie lines are tilted for $N_{\mathrm{AB}} < N_{\mathrm{B'C}}$ because it is harder for the larger B′C polymers to fit in the interstitial sites of the AB-rich bcc phase (Fig. 4a) than vice versa. The double-tangent construction for the bcc-bcc equilibrium is indicated, and the C15 phase appears to be almost co-tangent to this line at the scale of this inset. For visualization purposes, it is easier to subtract this tie line from the free energy (see Fig. S3). The inset of Fig. 3 and the relevant panel of Fig. S3 indicate that a narrow window of Laves phase stability should exist at $\phi_{\mathrm{AB}} \approx 0.538$. This value is reasonably close to the value $\phi_{\mathrm{AB}} = 0.577$ predicted from mixing bcc-type particles

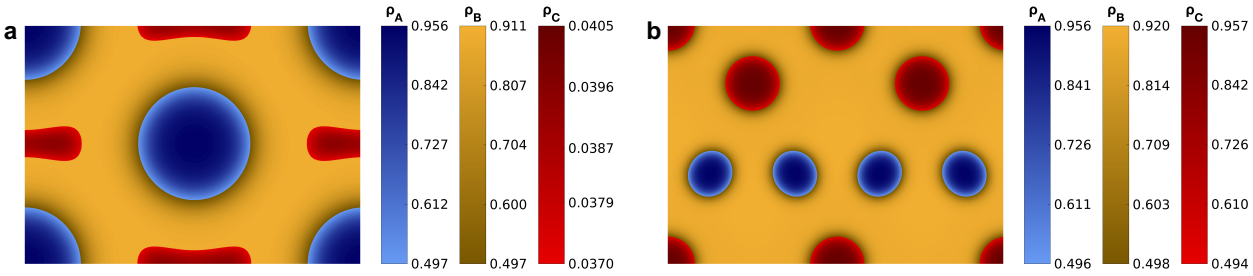

Figure 4: Density profiles for the [110] planes of (a) AB-rich bcc phase at $\phi_{AB} = 0.87$ and (b) C15 phase for $\phi_{AB} = 0.54$ for the conditions in the inset of Fig. 3. In panel (a), note that the density field ρ_C for bcc runs from 3.70% to 4.05% so that the impurity can be seen. For panel (b), the distortion of the smaller (blue) AB-rich C15 particles is evident from the shape of the A/B interface. The ratio of unit cell lattice parameters is $a_{C15}/a_{bcc} = 2.429$ but the figures have been drawn using the same unit cell size; when drawn to scale, the bcc and C15 particles are approximately the same size.

illustrated in Fig. 2. Naturally, the system must make some adjustments to both the particle shapes and aggregation numbers when forming C15, and we would not expect the bcc-based model to predict precisely the location of ϕ_{AB} for the Laves phase window. This distortion of the particles in the C15 packing can be understood by comparing the A/B interface for the bcc phase (Fig. 4a), which is essentially spherical,[60,61] to that in the C15 phase (Fig. 4b), where the (blue) AB-rich particles are distorted and the resulting A/B interface is ellipsoidal. Interestingly, the larger (red) B′C-rich particles in C15 retain the spherical B/C interface that they would exhibit in the bcc state. The ability of the micellar particles to exchange mass and reconfigure their shapes is an intrinsic feature of soft matter that differs from packing of hard spheres or atomic packing, and is very relevant to the stability of Frank-Kasper phases.[60]

The main panel of Fig. 3 summarizes the double-tangent construction results as a function of the ratio $N_{B'C}/N_{AB}$. When the two polymers have the same degree of polymerization, the system favors the formation of equal sized particles and the Laves phase has its highest free energy relative to the bcc-bcc coexistence. Interestingly, the data for $N_{B'C}/N_{AB} = 1.15$, which corresponds approximately to the volume asymmetry $\alpha = 1.23$ predicted for C15 from the Voronoi cell construction,[33] indicate a metastable Laves phase. In contrast, the

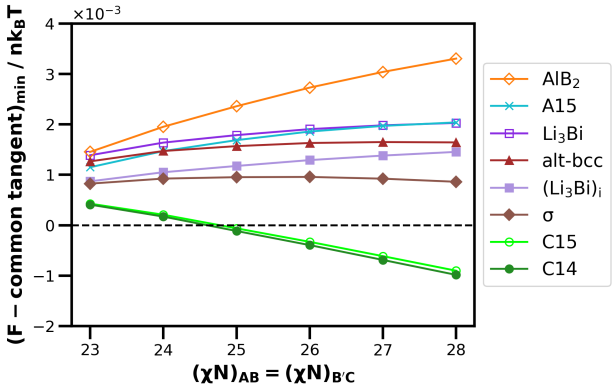

Figure 5: Comparison of the lowest free energy phases relative to the macrophase separation (bcc or fcc common tangent) as a function of the segregation strength where $\chi_{AC}N_{AB} = 2\,(\chi N)_{AB}$ for $N_{B'C}/N_{AB} = 1.3$ and $f_A = f_C = 0.2$. The data correspond, in order of ascending free energy at $(\chi N)_{AB} = 28$, to C14 (solid green circles), C15 (open light green circles), σ (solid brown diamonds), inverted Li_3Bi (solid light purple squares), alternating bcc (solid red-brown triangles), A15 (cyan x), Li_3Bi (open purple squares), and AlB_2 (open orange diamonds). For σ, which has five different particle volumes, the AB-chains are primarily located in the 2a and 8i Wyckoff positions. The free energy data for all competing phases as a function of ϕ_{AB} at each value of $(\chi N)_{AB}$ appear in Figs. S4-S9.

ratio $N_{B'C}/N_{AB} = 1.3$, which produces a volume ratio $\alpha = 1.48$ that is similar to what was obtained[60] for C15 from the unconstrained diblock foam model, appears to be the optimal degree of polymerization ratio. The robustness of the diblock foam model volume asymmetry[60] relative to the Voronoi construction here is consistent with recent criticisms of the Voronoi construction for Frank-Kasper phases.[62] Further increasing $N_{B'C}/N_{AB}$ leads to increasing free energy of the C15 phase relative to bcc-bcc coexistence until the Laves phase again becomes metastable. Based on these results, we selected the ratio $N_{B'C}/N_{AB} = 1.3$ (or, equivalently, $\alpha = 1.48$) as the system for further investigation.

While demonstrating that the Laves phase has a region of stability that would interrupt the bcc/bcc two-phase equilibrium, we also need to demonstrate that these are the only stable morphologies. To this end, we performed canonical ensemble SCFT calculations for 20 possible candidate phases (Table S2) that could plausibly produce crystals with two different particle sizes, inspired by the analysis of Shi and coworkers in the context of $B_1AB_2CB_3$ pentablock terpolymers.[63] Notably, this list of candidate phases includes C14 as a competing

Laves phase, as well as face-centered cubic (fcc) systems which, as expected,[56] proved to be stable at low segregation strengths and sufficiently high concentrations of minority species. These calculations were performed at different temperatures T by assuming that the Flory-Huggins parameter is purely enthalpic, i.e. where $\chi_{ij} = A_{ij}T_0/T$ with A_{ij} being a constant and T_0 a reference temperature. Continuing with the base case used in Fig. 3, this model corresponds to $A_{\mathrm{AB}} = 25$, $A_{\mathrm{BC}} = 19.23$ and $A_{\mathrm{AC}} = 50$.

Representative results for the free energies of all of the candidate phases in Table S2 for several values of T/T_0 are provided in Figs. S4-S9, with Fig. 5 providing a concise summary of the key results for the most stable phases. The Laves phase is the only state that outcompetes AB-rich or B′C-rich bcc or fcc at lower temperatures. However, at higher temperatures, the Laves phase becomes metastable because it becomes increasingly facile for the impurities to reside in the B-rich interstitial sites of bcc (or fcc) as χ_{AB} and χ_{BC} decrease, providing a favorable entropy of mixing without a substantial enthalpic cost. Moreover, these calculations revealed that C14 is the stable Laves phase but that it is nearly degenerate with C15, with a free energy difference of approximately $10^{-5}k_{\mathrm{B}}T$ per chain of size N_{AB} (Fig. S10). This near-degeneracy between C14 and C15 is expected from prior work.[17,18,32,59] Ultimately, distinguishing between these two very similar Laves phase particle packings is of little relevance in practice because fluctuation effects[12] and uncertainties in the experimental data (polydispersity, precision in measuring the degree of polymerization, mapping multiple χ parameters to experiments[64,65]) make it challenging to translate such subtle SCFT predictions into experimental realizations. For this reason, we will simply refer to the stable state as the "Laves" phase in what follows, with the understanding that SCFT predicts C14 but it is very plausible that C15 could be realized in practice.

To complete our analysis of this AB/B′C system, Fig. 6a provides the phase diagram as a function of temperature. Most of this figure was produced from double-tangent constructions of the canonical ensemble data presented thus far, but the more challenging regions of the phase diagram were computed from grand canonical ensemble calculations[56,58] using the

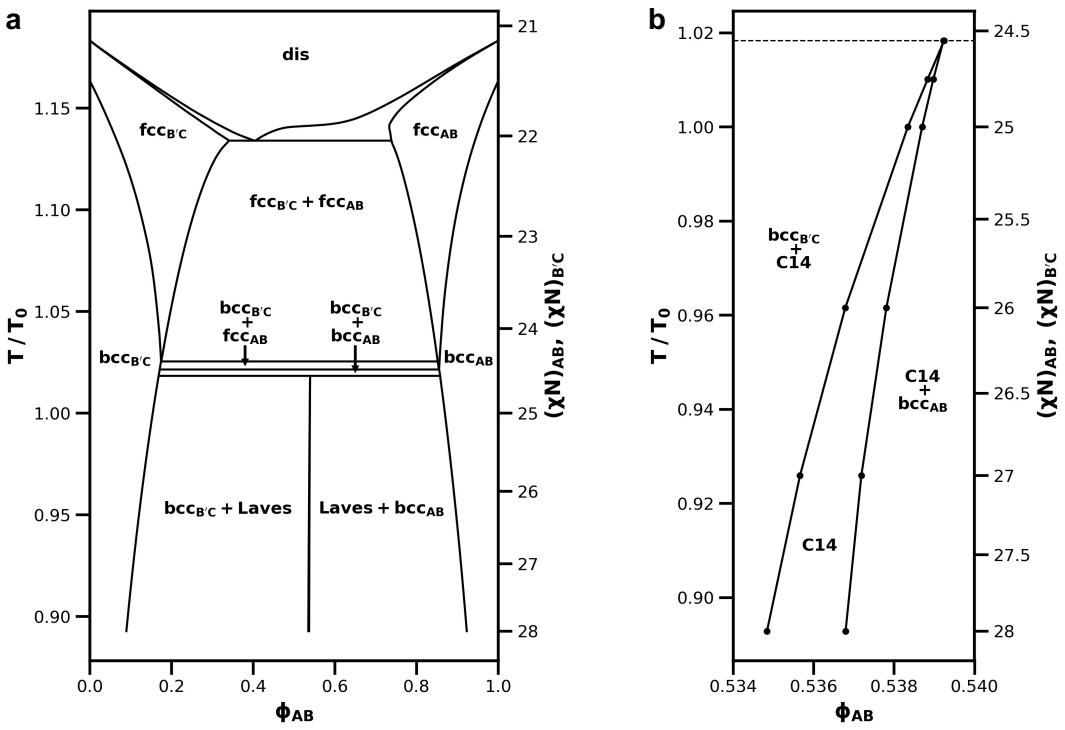

Figure 6: (a) Phase diagram for the AB/B′C blend for $N_{\mathrm{B'C}}/N_{\mathrm{AB}} = 1.3$, with $(\chi N)_{\mathrm{AB}} = (\chi N)_{\mathrm{B'C}}$ and $f_{\mathrm{A}} = f_{\mathrm{C}} = 0.2$. The reference temperature T_0 corresponds to $(\chi N)_{\mathrm{AB}} = 25$ and $\chi_{\mathrm{AC}} N_{\mathrm{AB}} = 50$; data at other temperatures were obtained by assuming χ is purely enthalpic, i.e. $\chi_{\mathrm{AC}} N_{\mathrm{AB}} = 2\,(\chi N)_{\mathrm{AB}}$. The state points used to compute this diagram are provided in Fig. S11, and an alternate view in terms of increasing χ values is provided in Fig. S12. (b) The details of the Laves phase field, which occupies an extremely narrow range in ϕ_{AB} at all temperatures examined here.

C++ version of PSCF;[66] see Fig. S1 for a comparison between methods. At the resolution of Fig. 6a, the Laves phase is effectively a line compound but, owing to the finite width illustrated by Fig. 6b, is denoted a phase field.[2] The emergence of a phase field, rather than a line compound, would be expected from the ability of block polymer micelles to exchange mass, which prevents their particles from adopting the fixed stoichiometry seen in metallic line compounds. Interestingly, the Laves phase field terminates before the eutectic as a result of the aforementioned ability of the impurities to more easily occupy the interstitial sites in bcc (see Fig. 4a) or fcc as the A/B and B/C repulsion is decreased. There is a significant asymmetry to the diagram due to the ratio of N_{AB} to $N_{\mathrm{B'C}}$, in particular near the eutectic point. In practice, however, we anticipate that fluctuations will cut off the upper part of the

phase diagram owing to the finite molecular weight polymers used in experiments.

Discussion

The results presented in this initial communication demonstrate the potential for alloying block polymers to stabilize volume-asymmetric particle packings, in this case for the C14 Laves phase, and to produce phase diagrams that closely mimic those occurring with metallic alloys. We posit that making this connection represents an important advance towards our overarching goal of understanding the similarities between Frank-Kasper phase formation in soft matter and metallic alloys.[33] In addition to its conceptual simplicity, the block polymer alloying approach that we have considered here has significant advantages in practice. SCFT has predicted many intriguing particle packing morphologies using multiblock polymers and nonlinear architectures.[63,67–70] One could envision, for example, how the $B_1AB_2CB_3$ system proposed previously to mimic metallic crystal structures[63] might be designed to produce a polymeric packing with a Laves phase volume asymmetry. While one-component systems are attractive because they avoid the complication of macroscopic phase separation, synthesizing these materials is not trivial,[71–74] especially if the predicted stability region occupies a narrow range in composition. Moreover, the ordering kinetics of multiblock polymers can be prohibitively slow.[75] By comparison, diblock copolymers are easily prepared using a variety of synthetic approaches (e.g., anionic, controlled free radical, and ring opening metathesis polymerization), opening up a significantly wider range of chemistries. And the precision required by our approach is relatively modest; uncertainties in the value of f_A or f_C can be compensated by blending at different values of ϕ_{AB}, a much simpler task than synthesizing and screening a library of multiblock polymers to identify one that produces a Laves phase. If we assume that a polymer blend can be prepared with a volume fraction uncertainty of circa 1%, then applying the lever rule over the two-phase bcc + Laves window suggests that this alloying approach should produce crystals that contain circa 97% Laves phase.

Moreover, the precise composition required could be identified based on a couple of blending experiments, assuming the system reaches equilibrium. Finally, in practice, nucleation and growth of small grains of the minority phase (bcc) is likely to be prohibitively expensive from a free energy perspective, thereby producing pure Laves phase.

We do not yet know the sensitivity of the initial results presented here to the system parameters (statistical segment lengths, minority block volume fractions, Flory-Huggins parameters), but we anticipate that they should be relatively robust given the underlying principle of producing two particle sizes and blending them at the proper stoichiometry. Our optimism is also supported by recent experimental results for complex particle phase formation, including the C14 Laves phase, in binary blends of mesoatoms[76,77] that rely on mixing giant molecules of different shapes that then aggregate into different particle types, and predictions that size dispersity in colloidal systems can stabilize Laves phases.[78]

Conclusions

We have used SCFT to establish the feasibility of stabilizing a C14 Laves phase in a diblock copolymer alloy formed by blending micelle-forming AB and B′C diblock polymers of different degrees of polymerization that promote the emergence of two distinct micelle sizes. The resulting phase diagram bears a striking resemblance to those observed in metallic alloys, with a Laves phase field, a eutectic point, and multiple regions of two-phase equilibria. While we have focused here on Laves phase formation, it is likely that this alloying approach will open up routes towards stabilizing other Frank-Kasper phases and other intermetallic-like packings with particle volume distributions and packings that are difficult to realize in single-component systems.[60]

Acknowledgement

We thank Akash Arora and David C. Morse for useful discussions. This work was supported by the National Science Foundation primarily through Award No. DMR-1719692 and partially through Award No. DMR-1725272 and the University of Minnesota Materials Science Research and Engineering Center under Award No. DMR-2011401. We acknowledge the Minnesota Supercomputing Institute (MSI) at the University of Minnesota for providing resources that contributed to the research results reported in this paper.

Supporting Information Available

Details of SCFT calculations; comparison of canonical and grand canonical calculations of two-phase equilibria; additional double-tangent constructions obtained for other values of $N_{\mathrm{B'C}}/N_{\mathrm{AB}}$; double-tangent constructions with subtraction of the tie lines; canonical ensemble results for all candidate phases at different segregation strengths; comparison of C14 and C15 free energies; phase diagram with discrete data points; phase diagram in terms of Flory-Huggins parameters. This material is available free of charge via the Internet at http://pubs.acs.org/.

References

(1) Callister Jr., W. D.; Rethwisch, D. G. *Materials Science and Engineering: An Introduction*; Wiley, 2014; Vol. 9.

(2) de Graef, M.; McHenry, M. E. *Structure of materials: An introduction to crystallography, diffraction, and symmetry*; Cambridge University Press: Cambridge, 2012; Vol. 2.

(3) Frank, F. C.; Kasper, J. S. Complex alloy structures regarded as sphere packings. I. Definitions and basic principles. *Acta Crystallogr.* **1958**, *11*, 184–190.

(4) Frank, F. C.; Kasper, J. S. Complex alloy structures regarded as sphere packings. II.

Analysis and classification of representative structures. *Acta Crystallogr.* **1959**, *12*, 483–499.

(5) Stein, F.; Leineweber, A. Laves phases: a review of their functional and structural applications and an improved fundamental understanding of stability and properties. *J. Mater. Sci.* **2020**, *56*, 5321–5427.

(6) Lindsay, A. P.; Mueller, A. J.; Mahanthappa, M. K.; Lodge, T. P.; Bates, F. S. Wigner-Seitz Cell generation and calculations in MATLAB. 2021; Retrieved from the Data Repository for the University of Minnesota, https://doi.org/10.13020/5bdw-8r09.

(7) Papadakis, C. M.; Almdal, K.; Mortensen, K.; Vigild, M. E.; Štěánek, P. Unexpected phase behavior of an asymmetric diblock copolymer. *J. Chem. Phys.* **1999**, *111*, 4319–4326.

(8) Uddin, M. H.; Rodriguez, C.; López-Quintela, A.; Leisner, D.; Solans, C.; Esquena, J.; Kunieda, H. Phase behavior and microstructure of poly(oxyethylene)-poly(dimethylsiloxane) copolymer melt. *Macromolecules* **2003**, *36*, 1261–1271.

(9) Lee, S.; Bluemle, M. J.; Bates, F. S. Discovery of a Frank-Kasper sigma phase in sphere-forming block copolymer melts. *Science* **2010**, *330*, 349–353.

(10) Chanpuriya, S.; Kim, K.; Zhang, J.; Lee, S.; Arora, A.; Dorfman, K. D.; Delaney, K. T.; Fredrickson, G. H.; Bates, F. S. Cornucopia of Nanoscale Ordered Phases in Sphere-Forming Tetrablock Terpolymers. *ACS Nano* **2016**, *10*, 4961–4972.

(11) Takagi, H.; Hashimoto, R.; Igarashi, N.; Kishimoto, S.; Yamamoto, K. Frank–Kasper σ phase in polybutadiene-poly(ϵ-caprolactone) diblock copolymer/polybutadiene blends. *J. Phys.: Condens. Matter* **2017**, *29*, 0204002.

(12) Bates, M. W.; Lequieu, J.; Barbon, S. M.; Lewis III, R. M.; Delaney, K. T.; Anas-

tasaki, A.; Hawker, C. J.; Fredrickson, G. H.; Bates, C. M. Stability of the A15 phase in diblock copolymer melts. *Proc. Natl. Acad. Sci. USA* **2019**, *116*, 13194–13199.

(13) Barbon, S. M.; Song, J.-a.; Chen, D.; Zhang, C.; Lequieu, J.; Delaney, K. T.; Anastasaki, A.; Rolland, M.; Fredrickson, G. H.; Bates, M. W.; Hawker, C. J.; Bates, C. M. Architecture Effects in Complex Spherical Assemblies of $(AB)_n$-Type Block Copolymers. *ACS Macro Lett.* **2020**, *9*, 1745–1752.

(14) Sun, Y.; Tan, R.; Gan, Z.; Li, G.; Zhou, D.; Shao, Y.; Zhang, W.-B.; Zhang, R.; Dong, X.-H. Discrete Block Copolymers with Diverse Architectures: Resolving Complex Spherical Phases with One Monomer Resolution. *ACS Cent. Sci.* **2020**, *6*, 1386–1393.

(15) Lindsay, A. P.; Lewis III, R. M.; Lee, B.; Peterson, A. J.; Lodge, T. P.; Bates, F. S. A15, σ, and a Quasicrystal: Access to Complex Particle Packings via Bidisperse Diblock Copolymer Blends. *ACS Macro Lett.* **2020**, *9*, 197–203.

(16) Yamamoto, K.; Takagi, H. Frank-Kasper and A-15 phases formed in symmetry and asymmetry block copolymer blend system. *Mater. Trans.* **2021**, *62*, 325–328.

(17) Kim, K.; Schulze, M. W.; Arora, A.; Lewis III, R. M.; Hillmyer, A.; Dorfman, K. D.; Bates, F. S. Thermal Processing of Diblock Copolymer Melts Mimics Metallurgy. *Science* **2017**, *356*, 520–523.

(18) Kim, K.; Arora, A.; Lewis, R. M.; Liu, M.; Li, W.; Shi, A.-C.; Dorfman, K. D.; Bates, F. S. Origins of low-symmetry phases in asymmetric diblock copolymer melts. *Proc. Natl. Acad. Sci. USA* **2018**, *115*, 847–854.

(19) Jeon, S.; Jun, T.; Jo, S.; Ahn, H.; Lee, S.; Lee, B.; Ryu, D. Y. Frank–Kasper Phases Identified in PDMS-b-PTFEA Copolymers with High Conformational Asymmetry. *Macromol. Rapid Commun.* **2019**, *40*, 1900259.

(20) Mueller, A. J.; Lindsay, A. P.; Jayaraman, A.; Lodge, T. P.; Mahanthappa, M. K.; Bates, F. S. Emergence of a C15 Laves Phase in Diblock Polymer/Homopolymer Blends. *ACS Macro Lett.* **2020**, *9*, 576–582.

(21) Lindsay, A. P.; Cheong, G. K.; Peterson, A. J.; Weigand, S.; Dorfman, K. D.; Lodge, T. P.; Bates, F. S. Complex phase formation in particle-forming AB/AB′ diblock copolymer blends with variable core block lengths. *Macromolecules* **2021**, *54*, 7088–7101.

(22) Nouri, B.; Chen, C.-Y.; Huang, Y.-s.; Mansel, B. W.; Chen, H.-L. Emergence of a Metastable Laves C14 Phase of Block Copolymer Micelle Bearing a Glassy Core. *Macromolecules* **2021**, *54*, 9195–9203.

(23) Vargas, R.; Mariani, P.; Gulik, A.; Luzzati, V. Cubic phases of lipid-containing systems. The structure of phase Q223 (Space group Pm3n). An X-ray scattering study. *J. Mol. Biol.* **1992**, *225*, 137–145.

(24) Luzzati, V.; Vargas, R.; Gulik, A.; Mariani, P.; Seddon, J. M.; Rivas, E. Lipid Polymorphism: A Correction. The Structure of the Cubic Phase of Extinction Symbol Fd–Consists of Two Types of Disjointed Reverse Micelles Embedded in a Three-Dimensional Hydrocarbon Matrix. *Biochemistry* **1992**, *31*, 279–285.

(25) Ungar, G.; Liu, Y.; Zeng, X.; Percec, V.; Cho, W.-D. Giant supramolecular liquid crystal lattice. *Science* **2003**, *299*, 1208–1211.

(26) Ungar, G.; Zeng, X. Frank–Kasper, quasicrystalline and related phases in liquid crystals. *Soft Matter* **2005**, *1*, 95–106.

(27) Huang, M.; Hsu, C.-H.; Wang, J.; Mei, S.; Dong, X.; Li, Y.; Li, M.; Liu, H.; Zhang, W.; Aida, T.; Zhang, W.-B.; Yue, K.; Cheng, S. Z. D. Selective assemblies of giant tetrahedra via precisely controlled positional interactions. *Science* **2015**, *348*, 424–428.

(28) Yue, K.; Huang, M.; Marson, R. L.; He, J.; Huang, J.; Zhou, Z.; Wang, J.; Liu, C.; Yan, X.; Wu, K.; Guo, Z.; Liu, H.; Zhang, W. B.; Ni, P.; Wesdemiotis, C.; Zhang, W. B.; Glotzer, S. C.; Cheng, S. Z. D. Geometry induced sequence of nanoscale Frank-Kasper and quasicrystal mesophases in giant surfactants. *Proc. Natl. Acad. Sci. USA* **2016**, *113*, 14195–14200.

(29) Kim, S. A.; Jeong, K. J.; Yethiraj, A.; Mahanthappa, M. K.; Jeong, J.; Yethiraj, A.; Mahanthappa, M. K. Low-symmetry sphere packings of simple surfactant micelles induced by ionic sphericity. *Proc. Natl. Acad. Sci. USA* **2017**, *114*, 4072–4077.

(30) Baez-Cotto, C. M.; Mahanthappa, M. K. Micellar Mimicry of Intermetallic C14 and C15 Laves Phases by Aqueous Lyotropic Self-Assembly. *ACS Nano* **2018**, *12*, 3226–3234.

(31) Su, Z.; Hsu, C.-h.; Gong, Z.; Feng, X.; Huang, J.; Zhang, R.; Wang, Y.; Mao, J.; Wesdemiotis, C.; Li, T.; Seifert, S.; Zhang, W.; Aida, T.; Huang, M.; Cheng, S. Z. D. Identification of a Frank-Kasper Z phase from shape amphiphile self-assembly. *Nat. Chem.* **2019**, *11*, 899–905.

(32) Magruder, B. R.; Dorfman, K. D. The C36 Laves phase in diblock polymer melts. *Soft Matter* **2021**, *17*, 8950–8959.

(33) Dorfman, K. D. Frank–Kasper Phases in Block Polymers. *Macromolecules* **2021**, *54*, 10251–10270.

(34) Cheong, G. K.; Bates, F. S.; Dorfman, K. D. Symmetry breaking in particle-forming diblock polymer/homopolymer blends. *Proc. Natl. Acad. Sci. USA* **2020**, *117*, 16764–16769.

(35) Xie, J.; Shi, A.-C. Formation of complex spherical packing phases in diblock copolymer/homopolymer blends. *Giant* **2021**, *5*, 100043.

(36) Xie, J.; Li, Y.; Shi, A.-C. Binary Blends of Diblock Copolymers: An Efficient Route to Complex Spherical Packing Phases. *Macromol. Theory Simulations* **2021**, 2100053.

(37) Liu, M.; Qiang, Y.; Li, W.; Qiu, F.; Shi, A.-C. Stabilizing the Frank-Kasper phases via binary blends of AB diblock copolymers. *ACS Macro Lett.* **2016**, *5*, 1167–1171.

(38) Ishizu, K.; Omote, A.; Fukutomi, T. Phase separation in binary block copolymer blends. *Polymer (Guildf).* **1990**, *31*, 2135–2140.

(39) Borovinskii, A. L.; Khokhlov, A. R. Microphase separation in a mixture of block copolymers in the strong segregation regime. *Macromolecules* **1998**, *31*, 1180–1187.

(40) Olmsted, P. D.; Hamley, I. W. Lifshitz points in blends of AB and BC diblock copolymers. *Europhys. Lett.* **1999**, *45*, 83–89.

(41) Kimishima, K.; Jinnai, H.; Hashimoto, T. Control of Self-Assembled Structures in Binary Mixtures of A-B Diblock Copolymer and A-C Diblock Copolymer by Changing the Interaction between B and C Block Chains. *Macromolecules* **1999**, *32*, 2585–2596.

(42) Vaidya, N. Y.; Han, C. D. Temperature-composition phase diagrams for binary blends consisting of chemically dissimilar diblock copolymers. *Macromolecules* **2000**, *33*, 3009–3018.

(43) Frielinghaus, H.; Hermsdorf, N.; Sigel, R.; Almdal, K.; Mortensen, K.; Hamley, I. W.; Messé, L.; Corvazier, L.; Ryan, A. J.; Van Dusschoten, D.; Wilhelm, M.; Floudas, G.; Fytas, G. Blends of AB/BC diblock copolymers with a large interaction parameter χ. *Macromolecules* **2001**, *34*, 4907–4916.

(44) Frielinghaus, H.; Hermsdorf, N.; Almdal, K.; Mortensen, K.; Messé, L.; Corvazier, L.; Fairclough, J. P.; Ryan, A. J.; Olmsted, P. D.; Hamley, I. W. Micro- vs. macrophase separation in binary blends of poly(styrene)-poly(isoprene) and poly(isoprene)-poly(ethylene oxide) diblock copolymers. *Europhys. Lett.* **2001**, *53*, 680–686.

(45) Papadakis, C. M.; Busch, P.; Weidisch, R.; Eckerlebe, H.; Posselt, D. Phase behavior of binary blends of chemically different, symmetric diblock copolymers. *Macromolecules* **2002**, *35*, 9236–9238.

(46) Asari, T.; Matsuo, S.; Takano, A.; Matsushita, Y. Three-phase hierarchical structures from AB/CD diblock copolymer blends with complemental hydrogen bonding interaction. *Macromolecules* **2005**, *38*, 8811–8815.

(47) Mao, H.; Arrechea, P. L.; Bailey, T. S.; Johnson, B. J.; Hillmyer, M. A. Control of pore hydrophilicity in ordered nanoporous polystyrene using an AB/AC block copolymer blending strategy. *Faraday Discuss.* **2005**, *128*, 149–162.

(48) Mao, H.; Hillmyer, M. A. Macroscopic samples of polystyrene with ordered three-dimensional nanochannels. *Soft Matter* **2006**, *2*, 57–59.

(49) Mao, H.; Hillmyer, M. A. Morphological behavior of polystyrene-block-polylactide/polystyrene-block-poly(ethylene oxide) blends. *Macromol. Chem. Phys.* **2008**, *209*, 1647–1656.

(50) Jeon, H. G.; Hudson, S. D.; Ishida, H.; Smith, S. D. Microphase and macrophase transitions in binary blends of diblock copolymers. *Macromolecules* **1999**, *32*, 1803–1808.

(51) Sun, L.; Ginorio, J. E.; Zhu, L.; Sics, I.; Rong, L.; Hsiao, B. S. Phase transitions and honeycomb morphology in an incompatible blend of enantiomeric polylactide block copolymers. *Macromolecules* **2006**, *39*, 8203–8206.

(52) Sun, L.; Zhu, L.; Rong, L.; Hsiao, B. S. Tailor-made onionlike stereocomplex crystals in incompatible, enantiomeric, polylactide-containing block copolymer blends. *Angew. Chemie - Int. Ed.* **2006**, *45*, 7373–7376.

(53) Tang, C.; Lennon, E. M.; Fredrickson, G. H.; Kramer, E. J.; Hawker, C. J. Evolution of block copolymer lithography to highly ordered square arrays. *Science* **2008**, *322*, 429–432.

(54) Xie, N.; Li, W.; Qiu, F.; Shi, A.-C. σ phase formed in conformationally asymmetric AB-type block copolymers. *ACS Macro Lett.* **2014**, *3*, 906–910.

(55) Matsen, M. W.; Schick, M. Stable and unstable phases of a diblock copolymer melt. *Phys. Rev. Lett.* **1994**, *72*, 2660–2663.

(56) Matsen, M. W. Stabilizing new morphologies by blending homopolymer with block copolymer. *Phys. Rev. Lett.* **1995**, *74*, 4225–4228.

(57) Arora, A.; Qin, J.; Morse, D. C.; Delaney, K. T.; Glenn, H.; Bates, F. S.; Dorfman, K. D. Broadly Accessible SCFT for Block Polymer Materials Discovery. *Macromolecules* **2016**, *49*, 4675–4690.

(58) Shi, A. C. Self-Consistent Field Theory of Inhomogeneous Polymeric Systems. In *Var. Methods Mol. Model.*; Wu, J., Ed.; Springer: Singapore, 2017; pp 155–180.

(59) Zhao, M.; Li, W. Laves Phases Formed in the Binary Blend of AB_4 Miktoarm Star Copolymer and A-Homopolymer. *Macromolecules* **2019**, *52*, 1832–1842.

(60) Reddy, A.; Buckley, M. B.; Arora, A.; Bates, F. S.; Dorfman, K. D.; Grason, G. M. Stable Frank-Kasper phases of self-assembled, soft matter spheres. *Proc. Natl. Acad. Sci. USA* **2018**, *115*, 10233–10238.

(61) Collanton, R. P.; Dorfman, K. D. Interfacial geometry in particle-forming phases of diblock copolymers. *Phys. Rev. Mater.* **2022**, *6*, 015602.

(62) Reddy, A.; Feng, X.; Thomas, E. L.; Grason, G. M. Block Copolymers beneath the Surface: Measuring and Modeling Complex Morphology at the Subdomain Scale. *Macromolecules* **2021**, *54*, 9223–9257.

(63) Xie, N.; Liu, M.; Deng, H.; Li, W.; Qiu, F.; Shi, A.-C. Macromolecular metallurgy of binary mesocrystals via designed multiblock terpolymers. *J. Am. Chem. Soc.* **2014**, *136*, 2974–2977.

(64) Arora, A.; Pillai, N.; Bates, F. S.; Dorfman, K. D. Predicting the phase behavior of ABAC tetrablock terpolymers: Sensitivity to Flory–Huggins interaction parameters. *Polymer* **2018**, *154*, 305–314.

(65) Willis, J. D.; Beardsley, T. M.; Matsen, M. W. Simple and Accurate Calibration of the Flory–Huggins Interaction Parameter. *Macromolecules* **2020**, *53*, 9973–9982.

(66) Cheong, G. K.; Chawla, A.; Morse, D. C.; Dorfman, K. D. Open-source code for self-consistent field theory calculations of block polymer phase behavior on graphics processing units. *Eur. Phys. J. E* **2020**, *43*, 15.

(67) Liu, M.; Xia, B.; Li, W.; Qiu, F.; Shi, A.-C. Self-assembly of binary mesocrystals from blends of BABCB multiblock copolymers and ABC triblock copolymers. *Macromolecules* **2015**, *48*, 3386–3394.

(68) Chen, L.; Qiang, Y.; Li, W. Tuning Arm Architecture Leads to Unusual Phase Behaviors in a $(BAB)_5$ Star Copolymer Melt. *Macromolecules* **2018**, *51*, 9890–9900.

(69) Dong, Q.; Li, W. Effect of Molecular Asymmetry on the Formation of Asymmetric Nanostructures in ABC-Type Block Copolymers. *Macromolecules* **2021**, *54*, 203–213.

(70) Zhao, B.; Wang, C.; Chen, Y.; Liu, M. Frank-Kasper phases self-assembled from linear $A_1B_1A_2B_2$ tetrablock copolymer. *Langmuir* **2021**, *37*, 5642–5650.

(71) Touris, A.; Lee, S.; Hillmyer, M. A.; Bates, F. S. Synthesis of tri- and multiblock polymers with asymmetric poly(ethylene oxide) end blocks. *ACS Macro Lett.* **2012**, *1*, 768–771.

(72) Touris, A.; Chanpuriya, S.; Hillmyer, M. A.; Bates, F. S. Synthetic strategies for the generation of ABCA′ type asymmetric tetrablock terpolymers. *Polym. Chem.* **2014**, *5*, 5551–5559.

(73) Radlauer, M. R.; Fukuta, S.; Matta, M. E.; Hillmyer, M. A. Controlled synthesis of ABCA′ tetrablock terpolymers. *Polymer (Guildf).* **2017**, *124*, 60–67.

(74) Bates, M. W.; Barbon, S. M.; Levi, A. E.; Lewis III, R. M.; Beech, H. K.; Vonk, K. M.; Zhang, C.; Fredrickson, G. H.; Hawker, C. J.; Bates, C. M. Synthesis and Self-Assembly of AB_n miktoarm star polymers. *ACS Macro Lett.* **2020**, *9*, 396–403.

(75) Radlauer, M. R.; Arora, A.; Matta, M. E.; Bates, F. S.; Dorfman, K. D.; Hillmyer, M. A. Order and disorder in ABCA′ tetrablock terpolymers. *J. Phys. Chem. B* **2020**, *124*, 10266–10275.

(76) Liu, Y.; Liu, T.; Yan, X.-y.; Guo, Q.-Y.; Wang, J.; Zhang, R.; Zhang, S.; Su, Z.; Huang, J.; Liu, G.-x.; Zhang, W.; Zhang, W.; Aida, T.; Yue, K.; Huang, M.; Cheng, S. Z. D. Mesoatom Alloys via Self-sorting Approach of Giant Molecules Blends. *Giant* **2020**, *4*, 100031.

(77) Yan, X.-Y.; Guo, Q.-Y.; Liu, X.-Y.; Wang, Y.; Wang, J.; Su, Z.; Huang, J.; Bian, F.; Lin, H.; Huang, M.; Lin, Z.; Liu, T.; Liu, Y.; Cheng, S. Z. D. Superlattice Engineering with Chemically Precise Molecular Building Blocks. *J. Am. Chem. Soc.* **2021**, *143*, 21613–21621.

(78) Bommineni, P. K.; Varela-Rosales, N. R.; Klement, M.; Engel, M. Complex Crystals from Size-disperse Spheres. *Phys. Rev. Lett.* **2018**, *122*, 128005.

Supporting Information for "Laves phase field in a diblock copolymer alloy"

Benjamin R. Magruder, So Jung Park, Ryan P. Collanton, Frank S. Bates, and Kevin D. Dorfman*

Department of Chemical Engineering and Materials Science, University of Minnesota – Twin Cities, 421 Washington Ave SE, Minneapolis, Minnesota 55455, USA

E-mail: dorfman@umn.edu

*To whom correspondence should be addressed

Contents

S1 Self-Consistent Field Theory (SCFT)

This section provides a brief summary of the SCFT formalism used in this paper for computing the phase behavior of AB/B′C blends within the Polymer Self-Consistent Field (PSCF) software package.[1] The methodology provided below is largely based on the description of canonical ensemble SCFT in Ref. 2 and the on-line documentation for PSCF.[3] Additional information on SCFT, in particular for grand canonical ensemble, was obtained from Refs. 4–6.

S1.1 Polymer model

The polymers are modeled as continuous Gaussian chains comprised of three monomer types, $i = \{\mathrm{A}, \mathrm{B}, \mathrm{C}\}$, that are polymerized into two different block polymers, $k = \{\mathrm{AB}, \mathrm{B'C}\}$. The AB chain consists of N_A A-monomers and N_B B-monomers for a total degree of polymerization $N_\mathrm{AB} = N_\mathrm{A} + N_\mathrm{B}$, while the B′C chain consists of $N_{\mathrm{B}'}$ B-monomers and N_C C-monomers for a total degree of polymerization $N_{\mathrm{B'C}} = N_{\mathrm{B}'} + N_\mathrm{C}$. In the model, the monomers are coarse-grained and occupy the same monomer volume ν, such that the volume fraction of the A-block in the AB chain is $f_\mathrm{A} = N_\mathrm{A}/N_\mathrm{AB}$ and the volume fraction of the C-block in the B′C chain is $f_\mathrm{C} = N_\mathrm{C}/N_{\mathrm{B'C}}$. The interaction between a monomer of type i and another monomer of type $j \neq i$ is given by the Flory-Huggins parameter χ_{ij}. For simplicity, we have assumed that the statistical segment lengths of each polymer are identical and given by b. The blend has an overall volume fraction ϕ_AB of the AB chains, with the volume fraction of B′C chains given by $\phi_{\mathrm{B'C}} = 1 - \phi_\mathrm{AB}$. The total system is incompressible and consist of n monomers in a volume V, such that $n = V/\nu$. The calculations performed here are unit-cell SCFT, where the volume V in the various integrals that appear below is the unit-cell volume and the system is assumed to be spatially periodic to produce the macroscopic volume.

In this formalism, there is considerable flexibility in the identification of a "monomer" since the model is continuous. The monomer simply refers to the amount of a polymer chain

that occupies the volume ν and does not need to correspond to a chemical repeat unit.[1] Indeed, the standard convention is to use $N = 1$ for a single-component system, and our calculations for this blend were performed using $N_{\mathrm{AB}} = 1$ and $N_{\mathrm{B'C}} \geq N_{\mathrm{AB}}$. With this choice, we can also interpret the value of n as the number of chains of length N_{AB}, which proves convenient for expressing the free energy per chain, rather than per coarse-grained monomer.

Conversion from such SCFT calculations to an experimental system requires connecting the values of χ_{ij}, b, and N_k to a particular experimental system by specifying some reference volume ν_{ref} and making appropriate conversions using the segment density and molecular weights of the blocks. This mapping has been discussed in a straightforward manner by Sinturel *et al.*[7]

S1.2 Statistical weights

The statistical weight of a given species k is computed by solving first a modified diffusion equation for the forward propagator $q_k(\mathbf{r}, s)$,

$$\frac{\partial q_k(\mathbf{r}, s)}{\partial s} = \left[\frac{b^2}{6}\nabla^2 - \omega_{i(s)}(\mathbf{r})\right] q_k(\mathbf{r}, s) \tag{S1}$$

which is a function of spatial position $\mathbf{r}$ and coordinate s along the chain contour. Here, $\omega_i(\mathbf{r})$ is a spatially-dependent chemical potential field that acts on monomer type i and given by

$$\omega_{\mathrm{A}} = \chi_{\mathrm{AB}}\rho_{\mathrm{B}}(\mathbf{r}) + \chi_{\mathrm{AC}}\rho_{\mathrm{C}}(\mathbf{r}) + \xi(\mathbf{r}) \tag{S2}$$

$$\omega_{\mathrm{B}} = \chi_{\mathrm{AB}}\rho_{\mathrm{A}}(\mathbf{r}) + \chi_{\mathrm{BC}}\rho_{\mathrm{C}}(\mathbf{r}) + \xi(\mathbf{r}) \tag{S3}$$

$$\omega_{\mathrm{C}} = \chi_{\mathrm{AC}}\rho_{\mathrm{A}}(\mathbf{r}) + \chi_{\mathrm{BC}}\rho_{\mathrm{B}}(\mathbf{r}) + \xi(\mathbf{r}) \tag{S4}$$

where $\rho_i(\mathbf{r})$ is the number density (local volume fraction) of monomer i, whose computation will be specified later in Eqs. S8-S10. The Lagrange multiplier $\xi(\mathbf{r})$ is selected to enforce incompressibility,

$$\rho_{\mathrm{A}}(\mathbf{r}) + \rho_{\mathrm{B}}(\mathbf{r}) + \rho_{\mathrm{C}}(\mathbf{r}) = 1 \tag{S5}$$

For the AB chain, we thus use ω_{A} for $s \in [0, N_{\mathrm{A}}]$ and ω_{B} for $s \in [N_{\mathrm{A}}, N_{\mathrm{AB}}]$. Equivalently, the propagator for the B′C chain uses ω_{B} for $s \in [0, N_{\mathrm{B}'}]$ and ω_{C} for $s \in [N_{\mathrm{B}'}, N_{\mathrm{B}'\mathrm{C}}]$. The initial condition for the forward propagator is $q(\mathbf{r}, 0) = 1$.

With the solution for the forward propagator, the partition function for each of the polymers is computed from

$$Q_k = \frac{1}{V} \int_V \mathrm{d}\mathbf{r}\, q_k(\mathbf{r}, N_k) \tag{S6}$$

Owing to the inhomogeneity of the block polymer, computation of the volume fractions ρ_k requires a solution for the backwards propagator, $q_k^\dagger(\mathbf{r}, s)$,[4] which obeys the modified diffusion equation

$$-\frac{\partial q_k^\dagger(\mathbf{r}, s)}{\partial s} = \left[\frac{b^2}{6}\nabla^2 - \omega_{i(s)}(\mathbf{r})\right] q_k^\dagger(\mathbf{r}, s) \tag{S7}$$

subject to the initial condition $q_k^\dagger(\mathbf{r}, N_k) = 1$. The probability of locating the segment of the chain contour coordinate s at some position $\mathbf{r}$ is proportional to the product $q(\mathbf{r}, s)q^\dagger(\mathbf{r}, s)$.[8]

Note that the local volume fractions are often denoted by the symbol $\phi_i(\mathbf{r})$,[2] which requires yet another symbol to define the overall volume fraction in the blend, e.g., $\bar{\phi}_k$. We prefer here to use the notation $\rho_i(\mathbf{r})$ for the local volume fractions and the standard symbol ϕ_k for the overall volume fraction in the blend to avoid the need to use the overbar notation in the main text figures.

S1.3 Canonical ensemble

In the canonical ensemble, the volume fraction ϕ_{AB} is specified. The volume fractions of the different monomer types are then computed from[6]

$$\rho_{\mathrm{A}}(\mathbf{r}) = \frac{\phi_{\mathrm{AB}}}{Q_{\mathrm{AB}}N_{\mathrm{AB}}}\int_0^{N_{\mathrm{A}}} \mathrm{d}s\, q_{\mathrm{AB}}(\mathbf{r},s)q^{\dagger}_{\mathrm{AB}}(\mathbf{r},s) \tag{S8}$$

$$\rho_{\mathrm{B}}(\mathbf{r}) = \frac{\phi_{\mathrm{AB}}}{Q_{\mathrm{AB}}N_{\mathrm{AB}}}\int_{N_{\mathrm{A}}}^{N_{\mathrm{AB}}} \mathrm{d}s\, q_{\mathrm{AB}}(\mathbf{r},s)q^{\dagger}_{\mathrm{AB}}(\mathbf{r},s) + \frac{\phi_{\mathrm{B'C}}}{Q_{\mathrm{B'C}}N_{\mathrm{B'C}}}\int_0^{N_{\mathrm{B'}}} \mathrm{d}s\, q_{\mathrm{B'C}}(\mathbf{r},s)q^{\dagger}_{\mathrm{B'C}}(\mathbf{r},s) \tag{S9}$$

$$\rho_{\mathrm{C}}(\mathbf{r}) = \frac{\phi_{\mathrm{B'C}}}{Q_{\mathrm{B'C}}N_{\mathrm{B'C}}}\int_{N_{\mathrm{B'}}}^{N_{\mathrm{B'C}}} \mathrm{d}s\, q_{\mathrm{B'C}}(\mathbf{r},s)q^{\dagger}_{\mathrm{B'C}}(\mathbf{r},s) \tag{S10}$$

The set of equations S1-S10 needs to be solved self-consistently for a choice of the unit cell geometry. To provide an initial guess for the chemical potential fields, we use the form-factor method.[2,9] All canonical calculations were performed using the Anderson Mixing iteration algorithm,[10–12] with an integration step size of $\mathrm{d}s = 0.01$ and an error threshold of 1×10^{-5}. The grid spacings for different phases are provided later in Table S2. In obtaining the self-consistent solution, the unit cell size is also relaxed.[12,13]

Once the self-consistent solution has been obtained in the optimal unit cell, the Helmholtz free energy per monomer is computed from[2]

$$\frac{F}{nk_{\mathrm{B}}T} = \frac{\phi_{\mathrm{AB}}}{N_{\mathrm{AB}}}\left(\ln\frac{\phi_{\mathrm{AB}}}{Q_{\mathrm{AB}}} - 1\right) + \frac{\phi_{\mathrm{B'C}}}{N_{\mathrm{B'C}}}\left(\ln\frac{\phi_{\mathrm{B'C}}}{Q_{\mathrm{B'C}}} - 1\right) - \frac{1}{V}\int \mathrm{d}\mathbf{r}\,(\omega_{\mathrm{A}}\rho_{\mathrm{A}} + \omega_{\mathrm{B}}\rho_{\mathrm{B}} + \omega_{\mathrm{C}}\rho_{\mathrm{C}}) + \frac{1}{V}\int \mathrm{d}\mathbf{r}\,(\chi_{\mathrm{AB}}\rho_{\mathrm{A}}\rho_{\mathrm{B}} + \chi_{AC}\rho_{\mathrm{A}}\rho_{\mathrm{C}} + \chi_{\mathrm{BC}}\rho_{\mathrm{B}}\rho_{\mathrm{C}}) \tag{S11}$$

where k_{B} is Boltzmann's constant and T is the absolute temperature. This free energy is readily converted to a free energy per chain by multiplying by some degree of polymerization N. For a blend, there are several possibilities and we choose to reference our free energies to a chain of size N_{AB}.

S1.4 Grand canonical ensemble

In the grand canonical ensemble, we specify the chemical potentials μ_{AB} and $\mu_{\mathrm{B'C}}$ rather than the volume fractions ϕ_{AB} and $\phi_{\mathrm{B'C}}$. The chemical potentials are related to the volume fractions by[6]

$$\exp\left(\frac{\mu_k}{k_{\mathrm{B}}T}\right) Q_k = \phi_k \tag{S12}$$

Since the volume fractions must sum to unity, the chemical potentials are not independent. We chose, without loss of generality, to set $\mu_{\mathrm{AB}} = 0$ in our calculations.

For the SCFT solution, the volume fractions are still computed using Eqs. S8-S10, but the prefactors ϕ_k/Q_k are replaced by $\exp(\mu_k/k_{\mathrm{B}}T)$ following Eq. S12. The problem requires again obtaining a self-consistent solution for Eqs. S1-S10 in an optimal unit cell. In the grand canonical calculations, the modified diffusion Eqs. S1 and S7 were solved using an Anderson mixing scheme,[12,14] optimizing the unit-cell sizes with stress relaxation, with an integration step of $\mathrm{d}s = 0.01$ for the chain contour and an error threshold of 1×10^{-5}. The grand canonical calculations were only used here to refine the phase diagram data in Figure 6 and were thus performed for C14, C15, fcc and bcc phases using the canonical ensemble solutions as initial guesses for the fields. The grid sizes used for the fcc and C15 phases are same as the canonical ensemble calculations as listed later in Table S2, and we used $96 \times 96 \times 96$ for the bcc phase and $96 \times 96 \times 156$ for the C14 phase when finding the onset value of $(\chi N)_{\mathrm{AB}}$ for the C14 phase out to two decimal points. The output of the grand canonical ensemble calculation are the blend volume fractions ϕ_{AB} and $\phi_{\mathrm{B'C}}$, obtained from Eq. S12, and the grand canonical free energy[15]

$$F_{\mathrm{g}} = -PV \tag{S13}$$

where P is the system pressure. The grand canonical free energy is related to the Helmholtz free energy by[6]

$$F_g = F - n_{\mathrm{AB}}\mu_{\mathrm{AB}} - n_{\mathrm{B'C}}\mu_{\mathrm{B'C}} \tag{S14}$$

where n_k is the number of chains of type k in the blend. Using Eq. S13 in Eq. S14 and noting that $n_k = \phi_k V/(N_k \nu) = n\phi_k/N_k$, we have

$$PV = -F + n\left(\frac{\phi_{\mathrm{AB}}\mu_{\mathrm{AB}}}{N_{\mathrm{AB}}} + \frac{\phi_{\mathrm{B'C}}\mu_{\mathrm{B'C}}}{N_{\mathrm{B'C}}}\right) \tag{S15}$$

The pressure can be expressed in a dimensionless form by dividing by $nk_{\mathrm{B}}T$,

$$\frac{P\nu}{k_{\mathrm{B}}T} = -\frac{F}{nk_{\mathrm{B}}T} + \frac{\phi_{\mathrm{AB}}}{N_{\mathrm{AB}}}\left(\frac{\mu_{\mathrm{AB}}}{k_{\mathrm{B}}T}\right) + \frac{\phi_{\mathrm{B'C}}}{N_{\mathrm{B'C}}}\left(\frac{\mu_{\mathrm{B'C}}}{k_{\mathrm{B}}T}\right) \tag{S16}$$

These dimensionless forms for the pressure, Helmholtz free energy, and chemical potentials in Eq. S16 correspond to the outputs of the PSCF code.[3]

S1.5 Computing two-phase equilibria

Two coexisting phases are in equilibrium if the pressure, temperature, and chemical potentials of each species are equal in both phases. In the canonical ensemble, the system is incompressible, which implies that the Helmholtz free energy is invariant to the addition of a constant pressure;[6] thus, the condition of equal pressure can always be satisfied, because the pressure in the incompressible canonical ensemble is arbitrary. Specifying the Flory-Huggins parameters χ_{ij} sets the temperature, so satisfying the equal temperature requirement for phase equilibrium is trivial. The condition of equal chemical potential is met by the common-tangent construction,[16] illustrated in Fig. S1a in the context of equilibrium between an AB-rich bcc (body-centered cubic) phase and a B′C-rich bcc phase, with C15 and disorder (dis) as competing phases. The bcc-bcc common tangent line was found by interpolating the free energy data for each phase (collected at increments of 0.005 in ϕ_{AB}) using a third-order spline curve that was forced to pass through each data point exactly. The Nelder-Mead minimization algorithm was then used to identify the compositions of the two coexisting bcc phases, $\phi^{\mathrm{I}}_{\mathrm{AB}}$ and $\phi^{\mathrm{II}}_{\mathrm{AB}}$, that place $F^{\mathrm{I}}(\phi^{\mathrm{I}}_{\mathrm{AB}})$ and $F^{\mathrm{II}}(\phi^{\mathrm{II}}_{AB})$ along a common tangent line with one another, where phase I and phase II are the AB-rich and B′C-rich bcc

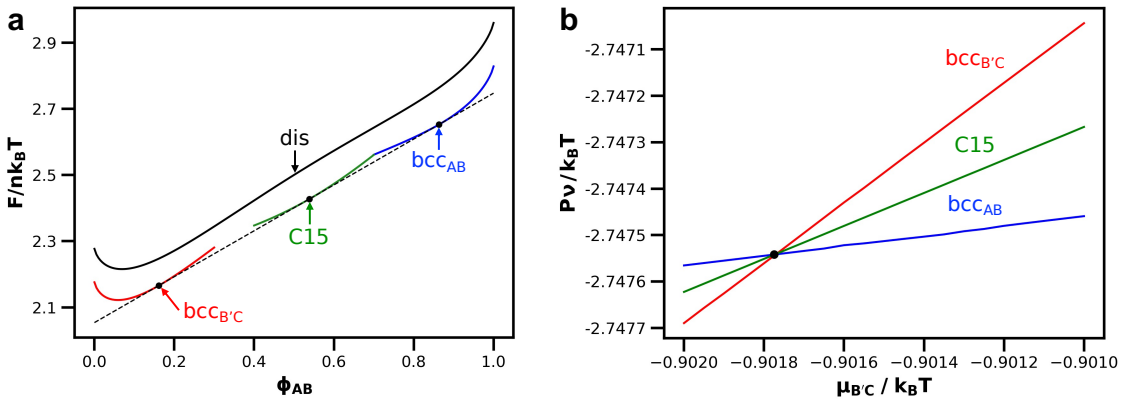

Figure S1: Comparison of (a) canonical and (b) grand canonical calculations for AB-rich bcc, B′C-rich bcc and C15 at $(\chi N)_{\mathrm{AB}} = (\chi N)_{\mathrm{B'C}} = 24.75$ and $\chi_{\mathrm{AC}} N_{\mathrm{AB}} = 49.5$. The canonical ensemble data were obtained at increments of 0.005 in ϕ_{AB} and the grand canonical data were obtained at increments of 5×10^{-5} in $\mu_{\mathrm{B'C}}/k_{\mathrm{B}}T$ with $\mu_{\mathrm{AB}} = 0$.

phases, respectively.

The approach for the grand canonical ensemble follows the method of Matsen,[4] noting that the equal temperature requirement is met by using the same Flory-Huggins parameters in each phase as was done for the canonical ensemble. Here, the chemical potential is provided as the input to the system, and the output is the system pressure from Eq. S16. To determine the equilibrium point, we use the degree of freedom in the chemical potential (Eq. S12) to first set $\mu_{\mathrm{AB}} = 0$, which automatically satisfies the equal chemical potential for the AB chain between the two phases. We then performed SCFT calculations at increments of 5×10^{-5} in $\mu_{\mathrm{B'C}}/k_{\mathrm{B}}T$ to determine the point where the curves for $P(\mu_{\mathrm{B'C}})$ intersect, which is the condition at which the remaining criteria for phase equilibrium (equal pressure and equal chemical potential for the B′C chain) are satisfied. Here, no interpolation was performed; with such small increments of $\mu_{\mathrm{B'C}}/k_{\mathrm{B}}T$, the compositions of each phase changed very little for each step, so the equilibrium compositions that we use are taken directly from the SCFT output at the value of $\mu_{\mathrm{B'C}}/k_{\mathrm{B}}T$ closest to the intersection point. Figure S1b illustrates this calculation for bcc-bcc equilibrium with C15 as a competing phase.

Figure S1 demonstrates the very good agreement between these two complementary approaches at $(\chi N)_{\mathrm{AB}} = (\chi N)_{\mathrm{B'C}} = 24.75$ and $\chi_{\mathrm{AC}} N_{\mathrm{AB}} = 49.5$, which is the point where

Table S1: Comparison of the volume fractions obtained from the data in Fig. S1.

Ensemble	ϕ_{AB} ($bcc_{B'C}$)	ϕ_{AB} (C15)	ϕ_{AB} (bcc_{AB})
Grand Canonical	0.161571	0.538207	0.863033
Canonical	0.161554	0.538169	0.863038

the C15 phase window effectively vanishes. The values of ϕ_{AB} corresponding to the AB-rich bcc phase, the B′C-rich bcc phase, and the values of ϕ_{AB} where C15 exists were determined by the common tangent method and by grand-canonical SCFT. Table S1 indicates that the results differed by less than 4×10^{-5}, demonstrating that either method will give the same results for two-phase equilibrium between ordered phases, even for this relatively challenging state point.

The grand canonical approach is generally preferred for computing phase behavior because it provides superior accuracy;[4] relatively large changes in the chemical potential produce small changes in the volume fractions, allowing one to precisely locate the equilibrium points using data similar to Fig. S1b. However, when there are many candidate phases, which is the case discussed in Section S3, it proves convenient to first use canonical ensemble calculations to identify the phase(s) of lowest free energy for subsequent grand canonical calculations. As suggested by Fig. S1, these canonical ensemble calculations were sufficient to resolve the phase behavior for ordered states in almost all cases. The main exception was the region close to the termination of the Laves phase window, where we used grand canonical SCFT to provide more detail for that point than can be achieved with canonical SCFT alone. However, our method for finding the common tangent also proved to be less reliable for finding two-phase equilibrium between an ordered state and the disordered state because the common tangent line was often very steep, and we used grand canonical SCFT for all such cases.

It is also worthwhile to recall a key point about the pressure and chemical potential produced from canonical ensemble calculations,[3,6] since this can be a source of confusion from the PSCF output. The dimensionless pressure in Eq. S16 and the chemical potential

in Eq. S12, while defined here in the discussion of the grand canonical ensemble, are computable from the canonical ensemble as well, and these quantities are output as part of the canonical ensemble calculation in PSCF. However, the Lagrange multiplier $\xi(\mathbf{r})$ in the canonical ensemble is only defined to within an arbitrary, additive constant and the Helmholtz free energy is independent of this choice.[3,6] The PSCF software uses the convention that the spatial average of $\xi(\mathbf{r})$ is zero,[3] rather than establishing the true pressure that would be associated with the given volume fraction ϕ_{AB}. As a result, the chemical potentials and pressures output from the canonical ensemble cannot be used to establish phase equilibria.

S2 Selecting an optimal ratio $N_{\mathrm{B'C}}/N_{\mathrm{AB}}$

As discussed in the main text, it is not immediately apparent what the ideal ratio of particle volumes α should be to stabilize a Laves phase in an AB/B′C diblock copolymer blend according to our "alloying" approach. The Voronoi construction predicts $\alpha \approx 1.23$,[17] while the unconstrained diblock foam model predicts a larger value $\alpha \approx 1.48$,[18] corresponding to polymer length ratios $N_{\mathrm{B'C}}/N_{\mathrm{AB}}$ of about 1.15 and 1.30, respectively.

To answer this question, we performed SCFT calculations using a variety of polymer length ratios. We first found the Helmholtz free energy curves for an AB-rich bcc micelle packing and a B′C-rich bcc packing as a function of AB volume fraction ϕ_{AB}. From these free energy curves, the common tangent construction was used to find the free energy of a two-phase mixture of the two bcc phases, which was compared to the free energy of the C15 Laves phase at the relevant compositions.

Figure S2 provides the original double-tangent constructions, analogous to the inset of Fig. 3 in the main text. In this presentation, it can be challenging to determine whether the Laves phase is below the tie line. Figure S3 thus provides the same data where the free energy of the bcc-bcc tie line, which is the free energy of the macrophase separated system, has been subtracted. The data in the main panel of Fig. 3 were computed using a third-order

spline fit to interpolate between data points in Fig. S3 and identify each minimum value for C15 precisely.

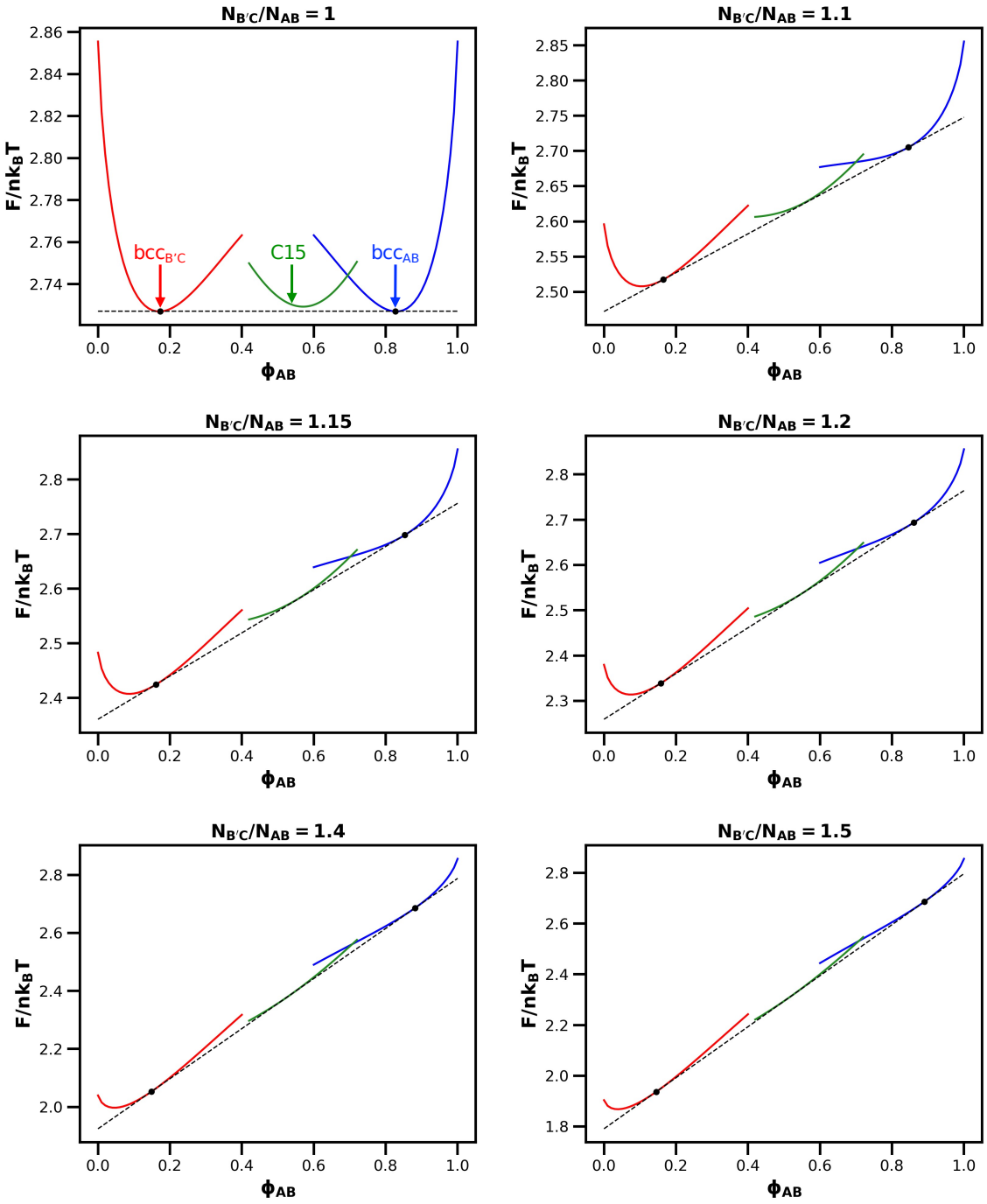

Figure S2: Free energy per chain of length N_{AB} for the AB/B′C blend at different values of $N_{\mathrm{B'C}}/N_{\mathrm{AB}}$, plotted as a function of the volume fraction of the AB diblock copolymer in the blend, ϕ_{AB}, for $f_{\mathrm{A}} = f_{\mathrm{C}} = 0.2$, $(\chi N)_{\mathrm{AB}} = (\chi N)_{\mathrm{B'C}} = 25$ and $\chi_{\mathrm{AC}} N_{\mathrm{AB}} = 50$. In all panels, the phases are, from left-to-right, B′C-rich bcc (red), C15 (green) and AB-rich bcc (blue) and these phases are labeled in the first panel. The bcc-bcc common tangent line is shown as a black dashed line, and the points of tangency are indicated with black dots. The data for $N_{\mathrm{B'C}}/N_{\mathrm{AB}} = 1.3$ appear in the inset of Fig. 3 of the main text.

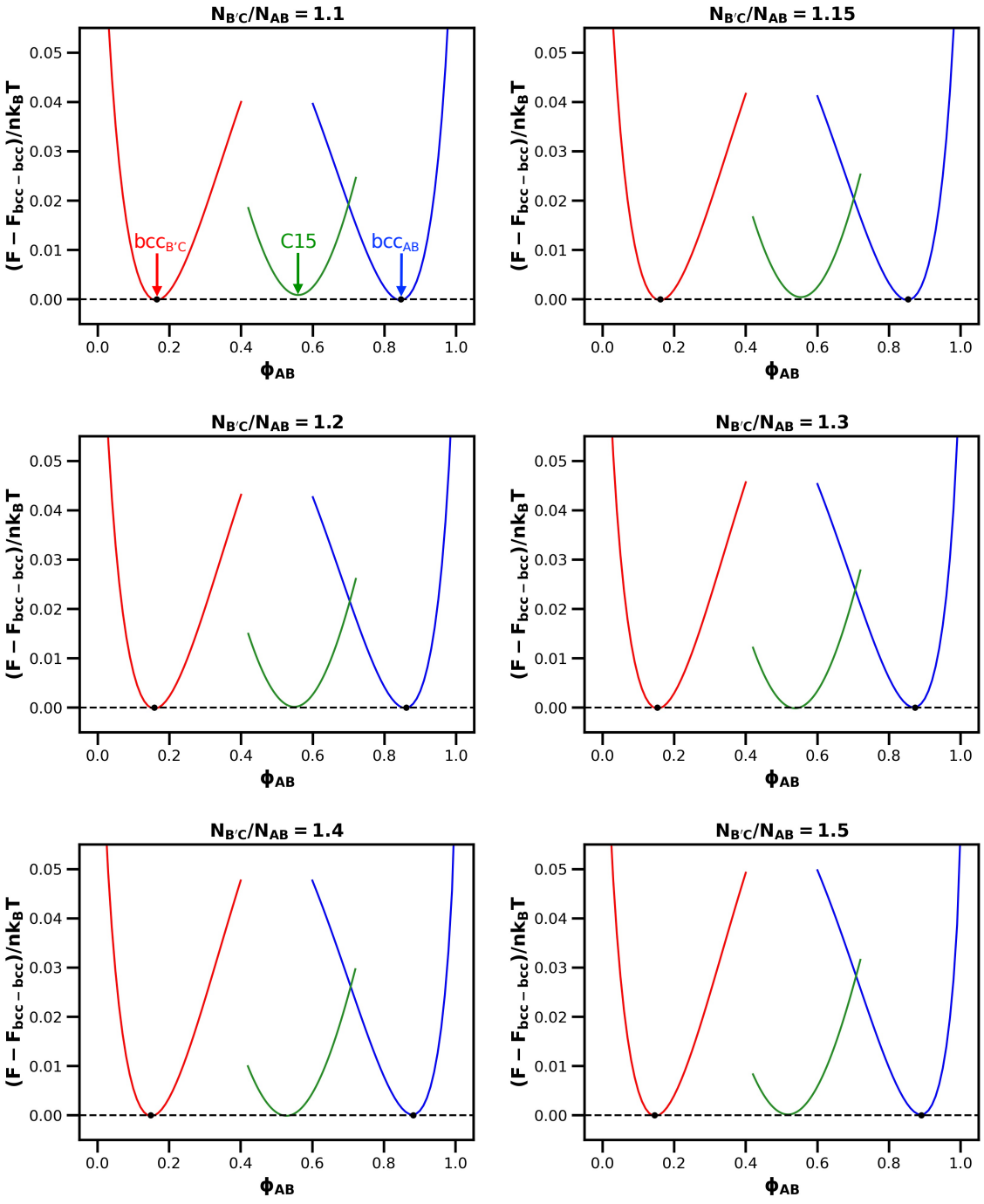

Figure S3: Same as Fig. S2 but with the common tangent, i.e., the free energy of the bcc-bcc macrophase separated system, subtracted from the data. The result for the symmetric system $N_{\mathrm{B'C}}/N_{AB} = 1.0$ is identical to the panel appearing in Fig. S2 and not reproduced in this figure.

S3 Free energies of different candidate phases

In order to be certain that our diblock copolymer alloying technique has truly stabilized the Laves phase, it is necessary to compute the free energy profiles of other candidate phases that may be stable in such a system. In Table S2, we provide information about each candidate phase that we considered, the majority of which are taken from the list of two-atom crystals that Xie *et al.*[19] predict will be stable phases in a pentablock terpolymer system $B_1AB_2CB_3$. For each phase, the table includes additional information about the crystal structure and its implementation in SCFT.

Figures S4-S9 provide the free energy diagrams at values of $(\chi N)_{AB} = (\chi N)_{B'C}$ from 23 to 28, with $\chi_{AC}N_{AB} = 2(\chi N)_{AB}$. In all cases, the blend has a ratio $N_{B'C}/N_{AB} = 1.3$, the block fractions are chosen such that $f_A = f_C = 0.20$ in neat melts of AB and B′C, and polymeric segments A, B, and C have identical statistical segment lengths b. All converged SCFT solutions are plotted. The figures reveal that the Laves phases are the only phases that are more stable than the bcc-bcc tie line, which is validation that the block copolymer alloying technique presented in this paper is working successfully. Figure 5 of the main text summarizes the most important results obtained from these figures, highlighting only the most stable phases.

S3.1 A note on convergence issues

Before showing the figures, it is important to comment on the candidate phases that presented SCFT convergence challenges in our diblock/diblock blend, specifically α-Al_2O_3, TiO_2, and ReO_3. In certain cases, these phases are omitted from the free energy profiles shown below, because convergence was not achieved. When the phases are included in the free energy profiles, the converged solutions have the problems described below.

α-Al_2O_3 and ReO_3 presented the same issue: each structure has a large void at the center of the unit cell, too large for our diblock blend to accommodate. In order to achieve

a converged SCFT solution, it is necessary for some polymers to be expelled from their micelles and settle into this void in the center of the unit cell, creating what is, in essence, another particle that is not part of the original structure. These expelled particles are small, and they contain a higher B-block volume fraction than the other particles, but they exist nonetheless and are worth noting. As a result of this problem, ReO_3 was particularly difficult to converge, and it is not shown on most of the figures below.

TiO_2 had a slightly different, but related, problem: in order to fill space evenly, all of the BC micelles need to be stretched into very oblong shapes that are nearly cylindrical in the middle, which is an unfavorable configuration. This made the phase very difficult to converge in SCFT.

It is reasonable to expect that these three phases would be especially difficult to converge in our blend system based on the results found by Xie *et al.*[19] for the $B_1AB_2CB_3$ architecture. For that pentablock terpolymer, all three of these phases are stable only in the case of a very long B_3 block (B_3 volume fraction of > 0.5). For such a polymer, it is reasonable to expect that stable structures could have both short interparticle distances (because of a short B_2 block) and large voids with no particles (occupied by the very long terminal B_3 block). For our AB/B′C blend, there does not exist an easy way to accommodate large voids like this, so we predict that these three structures will always be significantly less stable than the bcc-bcc tie line. Once could certainly construct a diblock copolymer alloy to attempt to stabilize these phases, but the diblocks in that system would look much different than those used here. As such, in the cases where convergence issues were encountered, the three phases discussed above are omitted from the free energy diagrams.

Table S2: Complete list of phases tested in our AB/B′C diblock copolymer blend, including relevant information about the structure of the phase and its implementation in canonical ensemble SCFT. For grand canonical calculations, some grid sizes are different and specified in Section S1.4.

Structure	**Alternate name**	**Particles per unit cell**	**Space Group**	**Crystal System**	**SCFT Grid Size**	**Ratio of AB to B′C particles**
$MgZn_2$	C14	12	P63/mmc	Hexagonal	64x64x104	2:1
$MgCu_2$	C15	24	$Fd\bar{3}m$	Cubic	96x96x96	2:1
W	bcc	2	$Im\bar{3}m$	Cubic	48x48x48	0 or 1*
CsCl	alt-bcc	2	$Pm\bar{3}m$	Cubic	64x64x64	1:1
Cu	fcc	4	$Fm\bar{3}m$	Cubic	48x48x48	0 or 1*
Hexagonally packed cylinders	hex	N/A	p6mm	Hexagonal	48x48	0 or 1*
Alternating hexagonally packed cylinders	alt-hex	N/A	p6mm	Hexagonal	48x48	2:1
Inverted alternating hexagonally packed cylinders	$(alt\text{-}hex)_i$	N/A	p6mm	Hexagonal	48x48	1:2
Nb_3Sn	A15	8	$Pm\bar{3}n$	Cubic	64x64x64	1:3
AlB_2	--	3	P6/mmm	Hexagonal	64x64x64	2:1
$\alpha\text{-}Al_2O_3$	sapphire	10	$R\bar{3}c$	Trigonal	64x64x64	3:2
α-BN	--	4	P63/mmc	Hexagonal	48x48x64	1:1
CaF_2	--	12	$Fm\bar{3}m$	Cubic	64x64x64	2:1
Li_3Bi	--	16	$Fm\bar{3}m$	Cubic	64x64x64	3:1
Inverted Li_3Bi	--	16	$Fm\bar{3}m$	Cubic	64x64x64	1:3
NaCl	rocksalt	8	$Fm\bar{3}m$	Cubic	64x64x64	1:1
ReO_3	--	4	$Pm\bar{3}m$	Cubic	64x64x64	3:1
σ-FeCr	σ	30	P42/mnm	Tetragonal	128x128x64	1:2**
TiO_2	--	6	P42/mnm	Tetragonal	64x64x42	1:2
ZnS	--	8	$F\bar{4}3m$	Cubic	64x64x64	1:1

*This structure does not have any particles of the minority species. The minority species thus occupies space in the interstitial sites only.

**This structure is not a two-atom crystal, so the choice of which particles to assign as AB diblocks is not obvious. The ratio given here, and used in our calculations, is chosen by identifying the largest gap in the particle size distribution from the unconstrained diblock foam model of Reddy *et al*. (18), which is between the 8i and 8j Wyckoff positions.

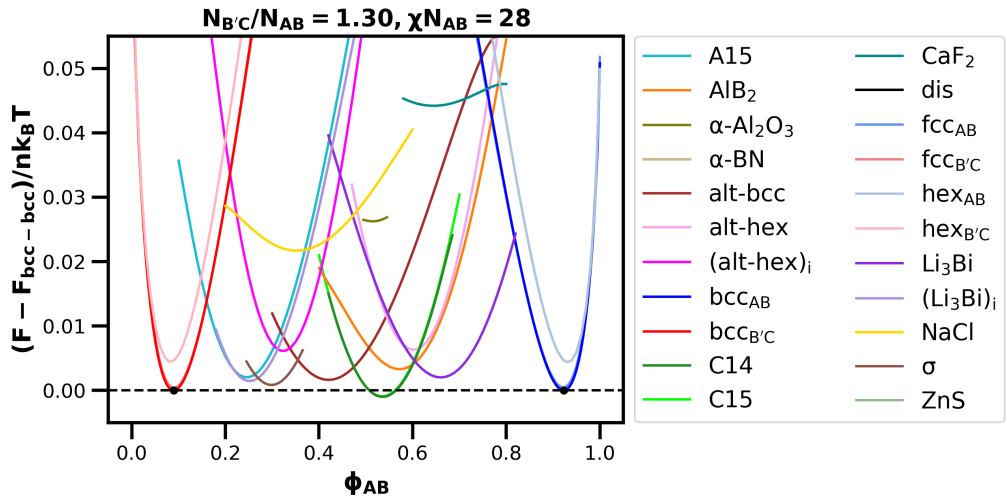

Figure S4: Free energy per chain of length N_{AB} relative to the bcc-bcc tie line for an AB/B′C blend of diblock copolymers, plotted as a function of the volume fraction of the AB diblock copolymer in the blend, ϕ_{AB}, for $f_{\mathrm{A}} = f_{\mathrm{C}} = 0.2$ and $N_{\mathrm{B'C}}/N_{\mathrm{AB}} = 1.3$. The segregation strengths are defined such that $(\chi N)_{\mathrm{AB}} = (\chi N)_{\mathrm{B'C}} = 28$ and $\chi_{\mathrm{AC}} N_{\mathrm{AB}} = 56$. The phases $\mathrm{fcc}_{\mathrm{AB}}$, $\mathrm{fcc}_{\mathrm{B'C}}$, and C15 are largely not visible because they are plotted underneath $\mathrm{bcc}_{\mathrm{AB}}$, $\mathrm{bcc}_{\mathrm{B'C}}$, and C14, respectively; in these overlapping instances, the phase that is plotted in front is the more stable of the two. The free energies of dis, α-BN, and ZnS are not visible because they are off of the top of the plot.

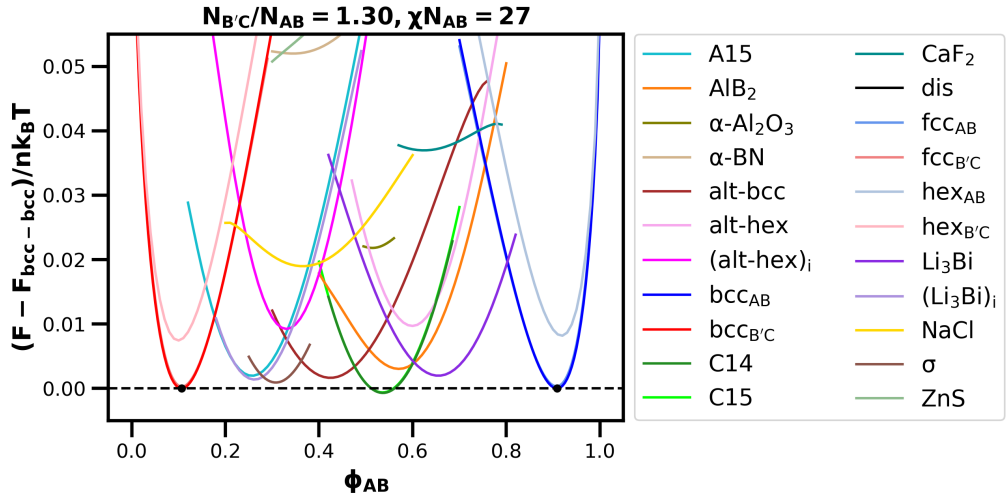

Figure S5: Identical to Figure S4, but with $(\chi N)_{\mathrm{AB}} = (\chi N)_{\mathrm{B'C}} = 27$ and $\chi_{\mathrm{AC}} N_{\mathrm{AB}} = 54$. $\mathrm{fcc}_{\mathrm{AB}}$, $\mathrm{fcc}_{\mathrm{B'C}}$, and C15 are largely not visible because they are plotted underneath $\mathrm{bcc}_{\mathrm{AB}}$, $\mathrm{bcc}_{\mathrm{B'C}}$, and C14, respectively; in these overlapping instances, the phase that is plotted in front is the more stable of the two. The free energy of dis is not visible because it is off of the top of the plot.

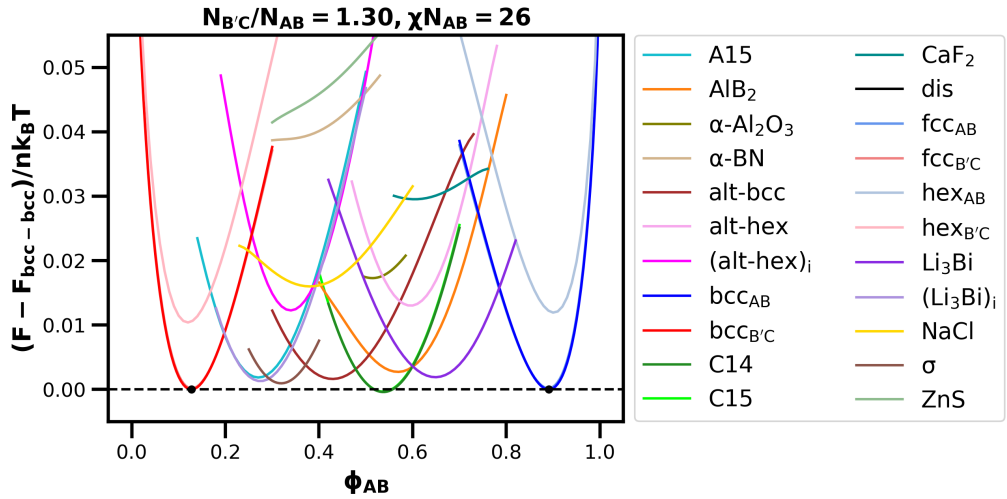

Figure S6: Identical to Figure S4, but with $(\chi N)_{\mathrm{AB}} = (\chi N)_{\mathrm{B'C}} = 26$ and $\chi_{\mathrm{AC}} N_{\mathrm{AB}} = 52$. $\mathrm{fcc}_{\mathrm{AB}}$, $\mathrm{fcc}_{\mathrm{B'C}}$, and C15 are largely not visible because they are plotted underneath $\mathrm{bcc}_{\mathrm{AB}}$, $\mathrm{bcc}_{\mathrm{B'C}}$, and C14, respectively; in these overlapping instances, the phase that is plotted in front is the more stable of the two. The free energy of dis is not visible because it is off of the top of the plot.

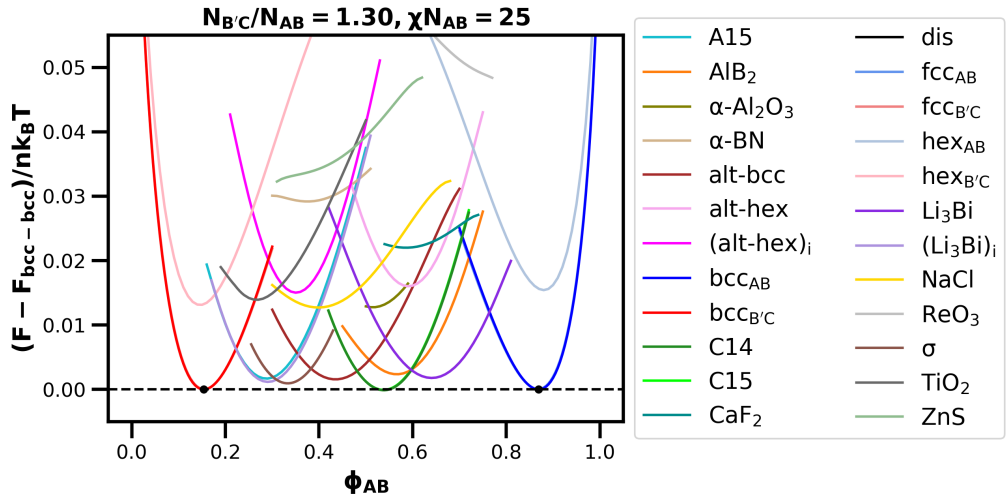

Figure S7: Identical to Figure S4, but with $(\chi N)_{\mathrm{AB}} = (\chi N)_{\mathrm{B'C}} = 25$ and $\chi_{\mathrm{AC}} N_{\mathrm{AB}} = 50$. $\mathrm{fcc_{AB}}$, $\mathrm{fcc_{B'C}}$, and C15 are largely not visible because they are plotted underneath $\mathrm{bcc_{AB}}$, $\mathrm{bcc_{B'C}}$, and C14, respectively; in these overlapping instances, the phase that is plotted in front is the more stable of the two. The free energy of dis is not visible because it is off of the top of the plot.

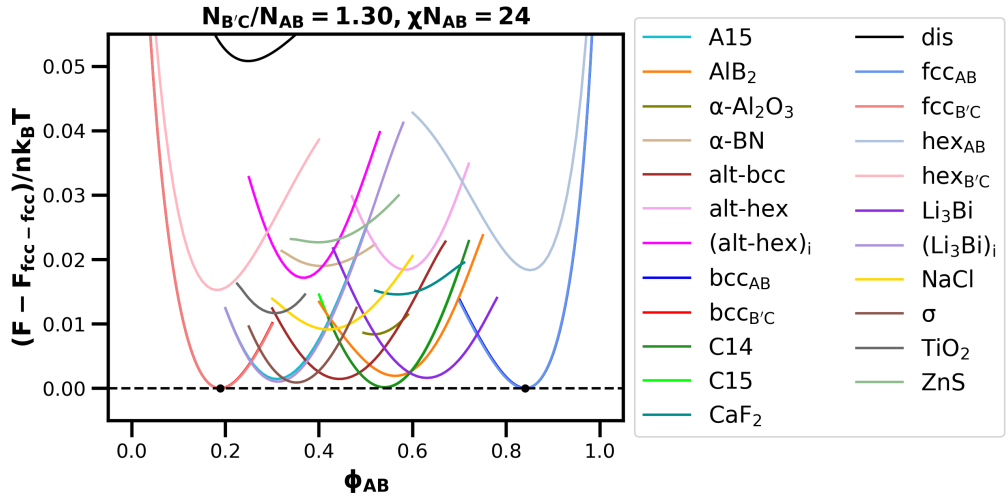

Figure S8: Identical to Figure S4, but with $(\chi N)_{\mathrm{AB}} = (\chi N)_{\mathrm{B'C}} = 24$ and $\chi_{\mathrm{AC}} N_{\mathrm{AB}} = 48$, and set relative to the fcc-fcc tie line instead of bcc-bcc. $\mathrm{bcc_{AB}}$, $\mathrm{bcc_{B'C}}$, and C15 are largely not visible because they are plotted underneath $\mathrm{fcc_{AB}}$, $\mathrm{fcc_{B'C}}$, and C14, respectively; in these overlapping instances, the phase that is plotted in front is the more stable of the two.

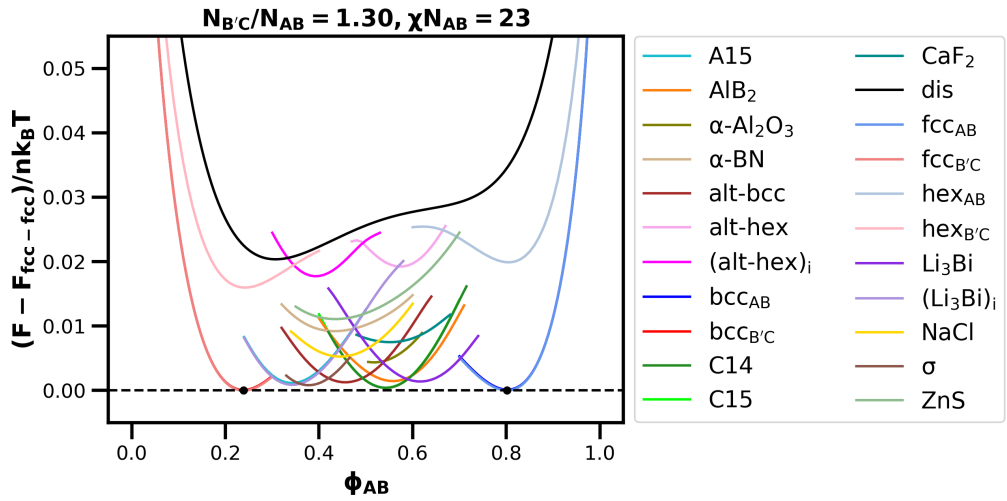

Figure S9: Identical to Figure S4, but with $(\chi N)_{\mathrm{AB}} = (\chi N)_{\mathrm{B'C}} = 23$ and $\chi_{\mathrm{AC}} N_{\mathrm{AB}} = 46$, and set relative to the fcc-fcc tie line instead of bcc-bcc. $\mathrm{bcc}_{\mathrm{AB}}$, $\mathrm{bcc}_{\mathrm{B'C}}$, and C15 are largely not visible because they are plotted underneath $\mathrm{fcc}_{\mathrm{AB}}$, $\mathrm{fcc}_{\mathrm{B'C}}$, and C14, respectively; in these overlapping instances, the phase that is plotted in front is the more stable of the two.

S3.2 Comparison of C14 and C15 free energies

Figure S10 summarizes the results for the C14 and C15 Laves phases over all of the conditions in Figs. S4-S9; owing to their near degeneracy, these two phases cannot be distinguished easily with the free energy scale used to display the results for all candidate phases. In all cases, the C14 phase is slightly more stable than the C15 phases in the mean-field limit. The difference is quite small in all cases, so the effects of fluctuations or dispersity in a real polymer system may be enough to stabilize C15 instead, and we prefer herein to refer to Laves phases as a degenerate set of phases for our intents and purposes. Interestingly, the two Laves phases become completely degenerate at about $\phi_{\mathrm{AB}} = 0.475$ at every temperature, but C15 never becomes more stable, which seems to be a result that occurs because of the similar symmetries of the structures. As our previous study shows,[20] the packing structure much more directly affects the free energy of a soft matter system than an analogous hard matter (metal alloy) system, so it makes sense that two very similar structures have a composition at which they are perfectly degenerate under all conditions in our polymer alloy.

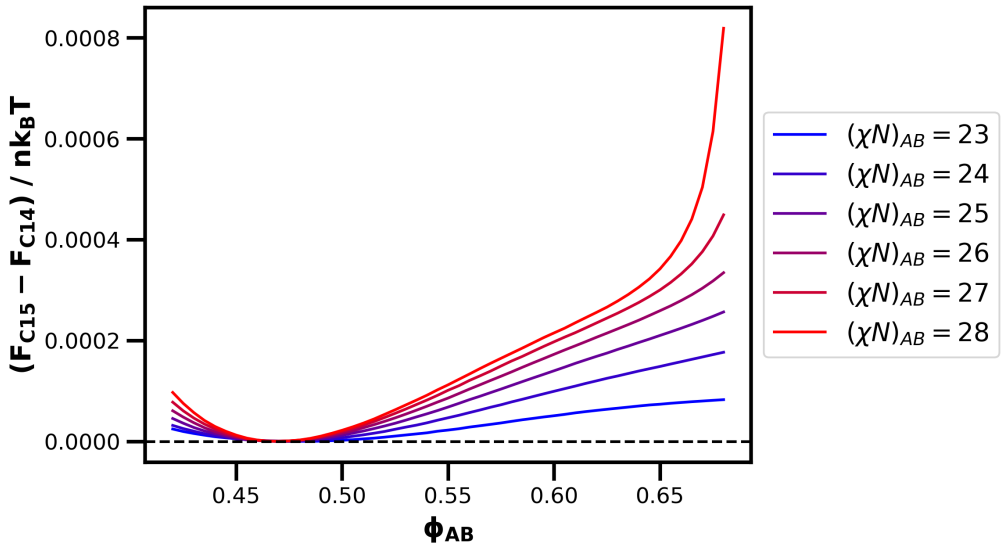

Figure S10: Free energy diagram showing the difference in free energy between the C15 and C14 phases for the system of Fig. 5 and Fig. 6 in the main text, as a function of the volume fraction of the AB diblock ϕ_{AB}. Data are shown at segregation strengths from $(\chi N)_{\mathrm{AB}} = (\chi N)_{\mathrm{B'C}} = 23$ to 28 with $\chi_{\mathrm{AC}} N_{\mathrm{AB}} = 2\,(\chi N)_{\mathrm{AB}}$.

S4 Construction of the phase diagram

Here, we present the details of the construction of the phase diagram shown in Figure 6 of the main text. Grand canonical SCFT calculations were used to determine the compositions in two-phase equilibrium with the disordered state (for $(\chi N)_{\mathrm{AB}} = (\chi N)_{\mathrm{B'C}} \leq 22.05$), because the common tangent lines became so steep so quickly that the error in compositions became large using the common tangent construction. At $(\chi N)_{\mathrm{AB}} = 22.05$, grand canonical SCFT gave the same compositions as the common tangent construction to within 0.001, so we used the common tangent construction for the remainder of the phase diagram. When temperature is sufficiently low to reach the onset of the Laves phase (for $(\chi N)_{\mathrm{AB}} = (\chi N)_{\mathrm{B'C}} \approx 24.6$), the difference between the results given by the two methods was less than 4×10^{-5} (Table S1), demonstrating that our methodologies are sound since they agree.

The figures in this section more closely explore the details of the phase diagram, and portray it in two different ways. First, in Figure S11, we show an alternate version of the phase diagram in which we have placed a dot at every point for which we have obtained SCFT data, to demonstrate that our data are sufficiently resolved that the spline interpolations used for Fig. 6 in the main text do not introduce any spurious artifacts. Owing the density of points required to resolve the phase boundary for disorder and bcc-fcc order-order transitions, we feel that the version appearing in Fig. 6 is the more effective presentation. Second, an alternate version of the phase diagram is provided in Figure S12 which is plotted with $(\chi N)_{\mathrm{AB}} = (\chi N)_{\mathrm{B'C}}$ as the main variable on the y-axis, with T/T_0 shown on the right hand axis. This is essentially just an inverted version of Fig. 6 of the main text, and conforms more closely to the typical theoretical representation of SCFT phase diagrams in terms of the Flory-Huggins parameters.

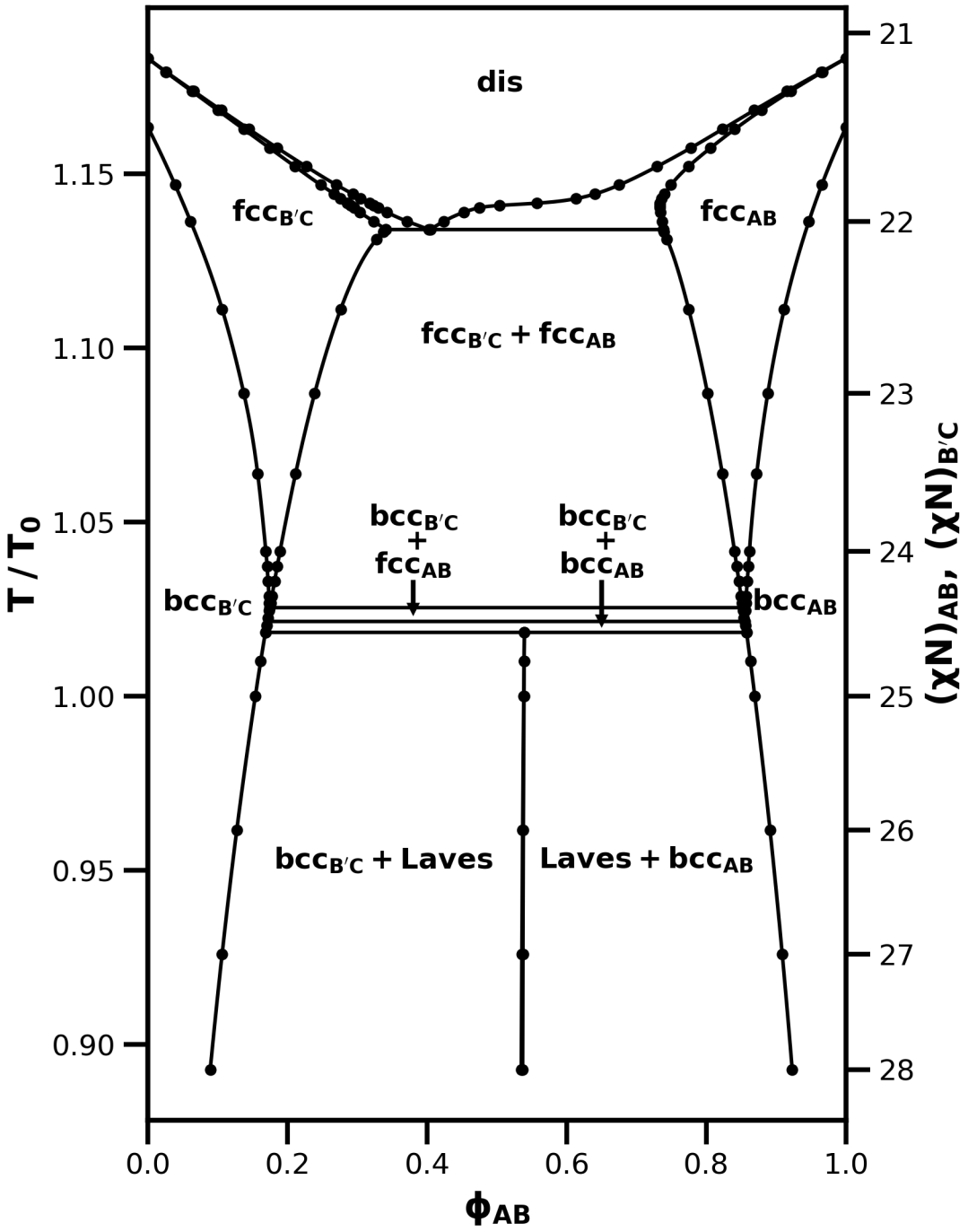

Figure S11: Identical to Figure 6 of the main text, but with a dot placed at each point for which we have obtained data. The lines are interpolated between data points using a third-order spline.

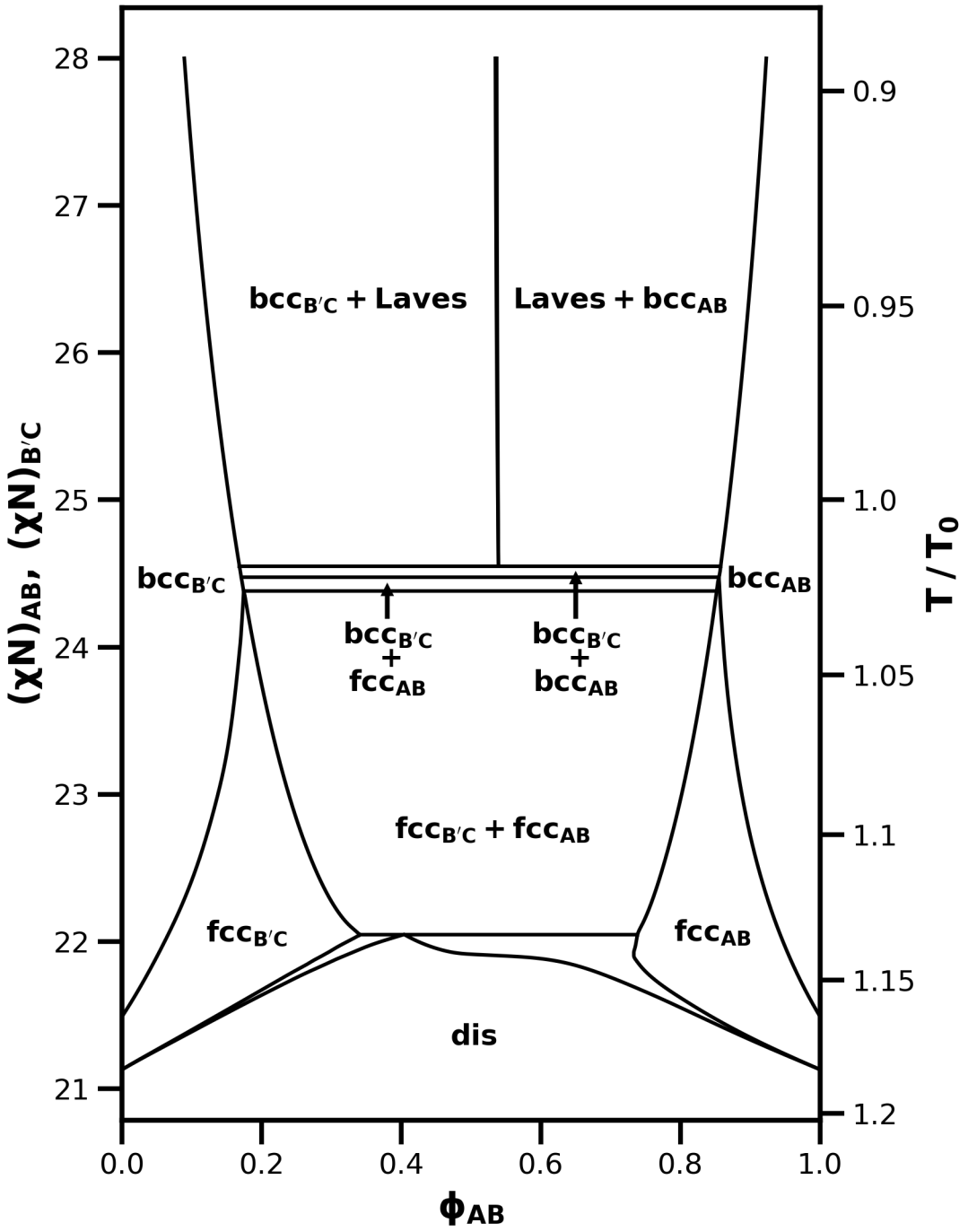

Figure S12: Identical to Figure 6 of the main text, but with the left and right y-axes switched. Here, it is plotted in terms of $(\chi N)_{\mathrm{AB}} = (\chi N)_{\mathrm{B'C}}$, with T/T_0 plotted on the right hand y-axis.

References

(1) https://github.com/dmorse/pscf. Accessed February 4, 2022.

(2) Arora, A.; Qin, J.; Morse, D. C.; Delaney, K. T.; Glenn, H.; Bates, F. S.; Dorfman, K. D. Broadly Accessible SCFT for Block Polymer Materials Discovery. *Macromolecules* **2016**, *49*, 4675–4690.

(3) https://readthedocs.org/projects/pscf/. Accessed February 4, 2022.

(4) Matsen, M. W. Stabilizing new morphologies by blending homopolymer with block copolymer. *Phys. Rev. Lett.* **1995**, *74*, 4225–4228.

(5) Matsen, M. W. Self-Consistent Field Theory and Its Applications. In *Soft Matter*; Gompper, G., Schick, M., Eds.; Wiley-VCH, 2007; Vol. 1: Polymer Melts and Mixtures; pp 87–178.

(6) Shi, A. C. Self-Consistent Field Theory of Inhomogeneous Polymeric Systems. In *Var. Methods Mol. Model.*; Wu, J., Ed.; Springer: Singapore, 2017; pp 155–180.

(7) Sinturel, C.; Bates, F. S.; Hillmyer, M. A. High χ–Low N Block Polymers: How Far Can We Go? *ACS Macro Lett.* **2015**, *4*, 1044–1050.

(8) Matsen, M. W. The standard Gaussian model for block copolymer melts. *J. Phys. Condens. Matter* **2002**, *14*, R21–R47.

(9) Case, L. J.; Delaney, K. T.; Fredrickson, G. H.; Bates, F. S.; Dorfman, K. D. Open-source platform for block polymer formulation design using particle swarm optimization. *Eur. Phys. J. E* **2021**, *44*, 115.

(10) Thompson, R. B.; Rasmussen, K. Ø.; Lookman, T. Improved convergence in block copolymer self-consistent field theory by Anderson mixing. *J. Chem. Phys.* **2004**, *120*, 31–34.

(11) Matsen, M. W. Fast and accurate SCFT calculations for periodic block-copolymer morphologies using the spectral method with Anderson mixing. *Eur. Phys. J. E* **2009**, *30*, 361–369.

(12) Arora, A.; Morse, D. C.; Bates, F. S.; Dorfman, K. D. Accelerating self-consistent field theory of block polymers in a variable unit cell. *J. Chem. Phys.* **2017**, *146*, 244902.

(13) Tyler, C. A.; Morse, D. C. Stress in Self-Consistent-Field Theory. *Macromolecules* **2003**, *36*, 8184–8188.

(14) Stasiak, P.; Matsen, M. W. Efficiency of pseudo-spectral algorithms with Anderson mixing for the SCFT of periodic block-copolymer phases. *Eur. Phys. J. E* **2011**, *34*, 110.

(15) McQuarrie, D. A. *Statistical thermodynamics*; Harper and Row: New York, 1973.

(16) Whitmore, M. D.; Noolandi, J. Theory of phase equilibria in block copolymerhomopolymer mixtures. *Macromolecules* **1985**, *18*, 2486–2497.

(17) Dorfman, K. D. Frank–Kasper Phases in Block Polymers. *Macromolecules* **2021**, *54*, 10251–10270.

(18) Reddy, A.; Buckley, M. B.; Arora, A.; Bates, F. S.; Dorfman, K. D.; Grason, G. M. Stable Frank-Kasper phases of self-assembled, soft matter spheres. *Proc. Natl. Acad. Sci. USA* **2018**, *115*, 10233–10238.

(19) Xie, N.; Liu, M.; Deng, H.; Li, W.; Qiu, F.; Shi, A.-C. Macromolecular metallurgy of binary mesocrystals via designed multiblock terpolymers. *J. Am. Chem. Soc.* **2014**, *136*, 2974–2977.

(20) Magruder, B. R.; Dorfman, K. D. The C36 Laves phase in diblock polymer melts. *Soft Matter* **2021**, *17*, 8950–8959.